FABRY-PEROT MODULATOR AND VERTICALLY INTEGRATED COUPLED CAVITY LIGHT EMITTING DIODE

A DISSERTATION
SUBMITTED TO THE DEPARTMENT OF APPLIED PHYSICS
AND THE COMMITTEE ON GRADUATE STUDIES
OF STANFORD UNIVERSITY
IN PARTIAL FULFILLMENT OF THE REQUIREMENTS
FOR THE DEGREE OF
DOCTOR OF PHILOSOPHY

By
Daxin Liu
December 1997

UMI Number: 9837228

UMI
300 North Zeeb Road
Ann Arbor, MI 48103

I certify that I have read this dissertation and that in my opinion it is fully adequate, in scope and quality, as a dissertation for the degree of Doctor of Philosophy.

James S. Harris, Ph.D.
(Principal Adviser)

I certify that I have read this dissertation and that in my opinion it is fully adequate, in scope and quality, as a dissertation for the degree of Doctor of Philosophy.

Robert L. Byer, Ph.D.

I certify that I have read this dissertation and that in my opinion it is fully adequate, in scope and quality, as a dissertation for the degree of Doctor of Philosophy.

Martin M. Fejer, Ph.D.

Approved for the University Committee on Graduate Studies:

Abstract

Fabry-Perot modulators with Multi-Quantum Well (MQW) cavities have been studied with great interest during recent years. Usually operating as intensity modulators, these devices have very high modulation contrast ratios, can be operated at very high speed, can be easily made into two dimensional arrays and can be integrated with silicon ICs. They are thus very promising for optical interconnects, optical switching and image processing applications. But, before these modulators are to be used in real applications, there are several issues that need to be solved; including elimination of parasitic phase modulation, increasing the optical bandwidth of such modulators and the precise alignment of modulator operating wavelength with the wavelength of lasers or light emitting diodes.

In this work, the phase properties of Fabry-Perot reflection modulators are first discussed and an experimental method using a modified Michelson interferometer to characterize the exact phase change is demonstrated. Measurements on modulators demonstrated that the phase of the reflection light beam from a Fabry-Perot modulator is determined not only by the refractive index change inside the cavity but also by the absorption change inside the cavity. With the purpose of expanding the limited optical bandwidth of such modulators, devices with short passive cavities were designed and fabricated. The results are described and trade-offs between modulation depth and optical bandwidth are discussed. In order to solve the problem of alignment and expand the functionality of Fabry-Perot modulators further, vertically coupled cavity devices, in which each cavity is electrically independently controlled have been developed. Both a coupled cavity modulator and an integrated light emitting diode with a transmission Fabry-Perot modulator are demonstrated; the first device enhances the modulation bandwidth while the second device has the potential of combining the advantage of high speed operation of MQW modulators with the long lifetime and low cost of light emitting diodes.

Acknowledgments

I would like to thank Professor James Harris for giving me the opportunity to join his group and for the support and guidance he provides throughout the years of my study. His knowledge of the field and his unique way of giving students freedom to pursue their interest have benefited me immensely.

I would like to thank Professor Robert Byer and Professor Martin Fejer, who are on my reading committee, for their helpful comments and suggestions regarding the writing of this dissertation. I would also like to thank Professor Huajian Gao for acting as my oral defense committee chairman upon last minute notice.

I would like to thank many fellow students in the Harris group for their help: Bardia Pezeshki showed me all the fundamentals of Fabry-Perot modulators and taught me a lot on the processing of optoelectronic devices and optical measurement techniques. Glenn Solomon, Herman Chui, and Baegin Sung helped me grow wafers on the MBE system. Mike Larson provided the thin-film computer simulation program that was very useful for the design process. I would like to thank all other members of the Harris group for their sharp questions, casual discussions, and all the hard work they contributed to keep all the equipment up and running.

I would also like to thank our administrative assistants Gail Chun-Creech and Lu Miao, who have helped make the whole group function smoothly.

I thank my wife Xuemei for her encouragement and support, which made my life at Stanford a wonderful experience.

This dissertation work was supported by a Shaw Fellowship and BMDO/ISTO through a grant with the Office of Naval Research.

Table of Contents

List of Tables

List of Figures

1 Introduction

Opto-electronic modulators are defined as electronically controlled devices that can change the properties of light. A prominent example of such a modulator is a liquid crystal display cell [1, 2], which combines with polarizers to modulate the intensity of transmission light by changing the refractive index of the liquid crystal with an applied electric field. Similar to liquid crystal cells, there are many other modulators that modulate the intensity of light and they are named as intensity modulators. There are also many other kinds of modulators that modulate other properties of light such as the phase [3], the polarization [4], and the frequency [5].

Semiconductor opto-electronic modulators are the focus of this research. Compared with other modulators such as liquid crystal cells and accousto-optic cells [6,7], semiconductor modulators have the advantages of higher speed of operation [8], smaller device size, and easier integration [9] with modern Integrated Circuit (IC) devices.

In real applications modulators are designed to work together with a constant light source. Depending on the configuration of the device, they can be characterized as waveguide (in-plane) modulators and vertical surface normal modulators. In general,

vertical modulators have several advantages over waveguide modulators, including the possibility of making them into high density 2-D arrays and the ease of fabrication [10]. In the past only the waveguide types of semiconductor modulators were feasible. This was because the physical effects of the bulk material [11,12] that were used to modulate light were all relatively weak, and with their much shorter active region, vertical modulators could not provide enough modulation strength. In a waveguide configuration the interaction length of a modulator could be quite long, hence adequate to compensate the weak effect. With the development of material growth technology in semiconductors such as Molecular Beam Epitaxy [13,14], a new class of materials, Multiple Quantum Wells [15], were discovered. These new materials have a very strong electro-absorption effect, namely the Quantum Confined Stark Effect [16]. The giant absorption change from this effect makes semiconductor vertical modulators possible.

Such vertical modulators have promising applications in several areas. The first area is for interconnects in optical communications network [2]. With the increasing demand of Internet and traditional telephone service, the volume of traffic is growing dramatically and switching these signals is a great challenge for traditional electronics due to the speed limitations and the fan-in / fan-out restriction. With the vertical modulators, free space switching provides great potential for fast and reliable switching.

The second area of application for vertical modulators is in optical data links in a computer [17]. With the exponentially increasing speed of modern computer CPUs, the input/output process is the bottleneck of the total process. On a single computer board, the input/output speed is fundamentally limited by the basic RC time constant of large conduction metal area, with the typical speed of system bus at only about one fifth of the speed of the CPU. One solution is to use on chip optoelectronic lasers/modulators to speed up the I/O process. In a larger scale, data links between different boards inside a computer

can also be dramatically improved by adopting modulator based optoelectronic communication.

There are several issues to be addressed before these modulators can be applied in the above applications and this thesis work focuses on two major factors. The first one is the parasitic phase modulation in an intensity modulator, which is extremely detrimental for high speed data communications applications. Prior to this work, there was no reliable way to measure and characterize the phase properties of vertical Fabry-Perot reflection modulators. An interferometer set-up was designed and used to experimentally measure the change of phase during the modulation process. Careful analysis shows that the phase behavior is under the joint influence of both the refractive index change inside the cavity and the absorption change inside the cavity. The results and the analysis of these factors will be discussed in detail in chapter 3.

The second issue is the optical bandwidth of these vertical modulators. A broad optical bandwidth is helpful in improving manufacturing tolerance of wavelength alignment, especially when these modulators are used with narrow linewidth lasers or light emitting diodes. In general, the optical bandwidth of a vertical modulator is determined by the cavity length and the mirror reflectivity. In conventional vertical modulators, the bandwidth is limited by the compromise between cavity length and mirror reflectivity. In this study, we explored three ways to circumvent this problem. First, a new scheme of short cavity modulators with inactive material and active mirrors are designed to provide broader optical bandwidth. Three different configurations of such short cavity devices are demonstrated and the trade-off between modulation efficiency and optical bandwidth are discussed in chapter 4.

Another approach of improving optical bandwidth is to incorporate an extra cavity into the modulator structure and the coupling between two cavities yields two Fabry-Perot bands that can be modulated in the same manner as one single band. A twin cavity device is

demonstrated. Its results and the characteristics of coupling between cavities is investigated and discussed in chapter 5.

A completely new way to solve the optical bandwidth problem is to eliminate the need for wavelength alignment by integrating the light source and the modulator into one device. The coupled cavity structure discussed in Chapter 5 can be configured as such a device, in which one of the cavity is designed as a light emitting diode and the other cavity is a modulator. By electrically contacting each device individually, the whole device functions as a signal source, with the light emitting diode set at a constant output power level and the output light modulated by the modulator. This device totally eliminates the need to increase the optical bandwidth of the vertical modulator since it does not require wavelength alignment with the light source, whose alignment is now integrated in the design. This device combines the benefits of both the fast speed, low power properties of vertical modulators and the low cost, long lifetime properties of light emitting diodes, and it points to a promising solution for future low cost, short distance optical data link applications.

2 Background

2.1 Quantum Wells and Quantum Confined Stark Effect

2.1.1 Quantum Well Material

In all the modulators in this study, Multiple Quantum Wells (MQW)[15] material and the Quantum Confined Stark Effect (QCSE) [16] are utilized. Multiple Quantum Wells material are two or more kinds of semiconductor material epitaxially grown in an alternating layered structure with typical layer thickness around 10nm. In a typical material system, GaAs/AlAs [18], the lower bandgap GaAs is sandwiched between layers of higher bandgap AlAs, and electronic energy wells are formed in the conduction band and valence band. The behavior of electrons and holes in such a material system can be treated similarly to the simple one dimensional particle in a box quantum well problem in quantum mechanics [19]. The electrons and holes each have their own set of energy levels above (electrons) or below (holes) the bottom of the corresponding energy band. Due to the Coulomb interaction between them, excitons are formed for all pairs of electrons and holes, and the resulting optical transition has a slightly lower energy than the energy difference between the

corresponding electron and hole levels. In the mean time the oscillator strength of optical absorption is greatly enhanced by this exciton effect simply because of the increase in the probability of finding electrons and holes at the same spatial location.

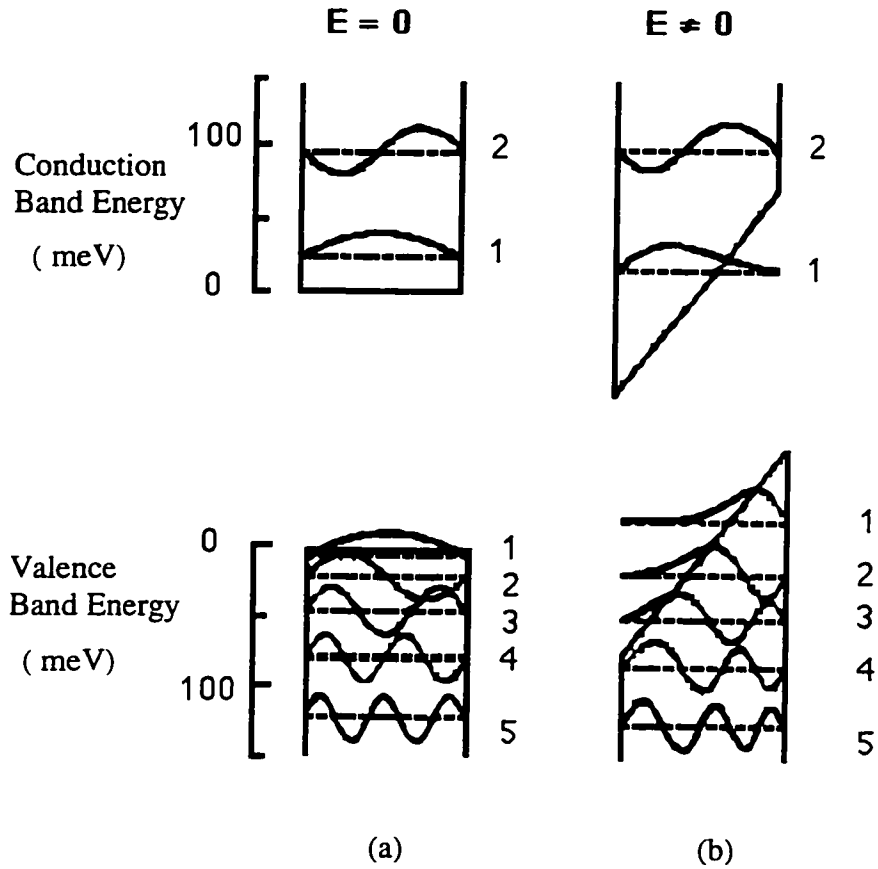

Figure 2.1 The first few energy levels of electrons and holes in an infinitely deep quantum well and the corresponding wavefunctions. (a) No electric field on the quantum well. (b) The electric field on the quantum well is nonzero.

Figure 2.1(a) shows the electron and hole wavefunctions of the first few energy levels in an infinitely deep quantum well under zero electric field (E = 0). The wave functions are sinusoidal functions that are symmetric about the center of the quantum well, therefore the overlap between the wavefunctions of the first electron level and the first hole

level wavefunctions is very strong. This results in high optical absorption strength between these two levels.

2.1.2 Quantum Confined Stark Effect

As shown in Figure 2.1 (b), when an electric field is applied across a quantum well structure ($E \neq 0$), the electron and hole wavefunction became asymmetric Airy functions while the energy levels of electrons and holes are shifted. The overlap between the wavefunctions of the first electron level and the first hole level is reduced, which leads to reduced optical absorption strength between them. However, due to the confinement of the energy barrier from the barrier material, field ionization of excitons is much less than in the bulk material. The result is that there is still a large exciton absorption available, albeit at a longer wavelength. This shift of exciton absorption peak yields large absorption changes over a large wavelength range at room temperature. This phenomenon is the Quantum Confined Stark Effect (QCSE).

Figure 2.2 shows the absorption spectra of a 30 period GaAs/AlAs MQW sample under three electric field levels. Under zero bias voltage, the electron heavy hole exciton absorption peak is at 830nm, marked as λ_0 in Figure 2.2 . When the bias voltage increases to 7.5V, the exciton peak position shifts to a longer wavelength of 845nm while its peak value drops from approximately 28000 cm^{-1} to approximately 16000 cm^{-1}, with some broadening of the peak as well. As the voltage goes up to 15V, the exciton peak shifts further to 873nm, and peak absorption drops to approximately 7000 cm^{-1} with further broadening of the exciton peak. It is clear from Figure 2.2 that there is a significant wavelength range where large absorption changes of over 5000 cm^{-1} can be realized. As pointed out by the arrows, the region between 840nm and 875nm and the region around 830nm are suitable. These two wavelength ranges [20] are commonly used in modulator designs, shown as λ_0 and λ_1 in Figure 2.2. At λ_0, where the zero bias exciton peak

occurs, the absorption level is very high at zero electric field, and goes down with applied field. At λ_1, where the shifted exciton peak occurs, the absorption level starts close to zero at zero electric field and increases with increasing electric field. The λ_0 region is primarily used in SEED devices [21] due to the drop in absorption with increasing field, while the λ_1 region is used in modulators because of the low absorption at zero bias.

In Fabry-Perot vertical modulators, for which high contrast ratio is desirable, the absorption at λ_1 is normally used because the absorption level is minimal when the field is low, which results in better contrast ratio [22,23]. We designed all the modulators in this study to operate at λ_1.

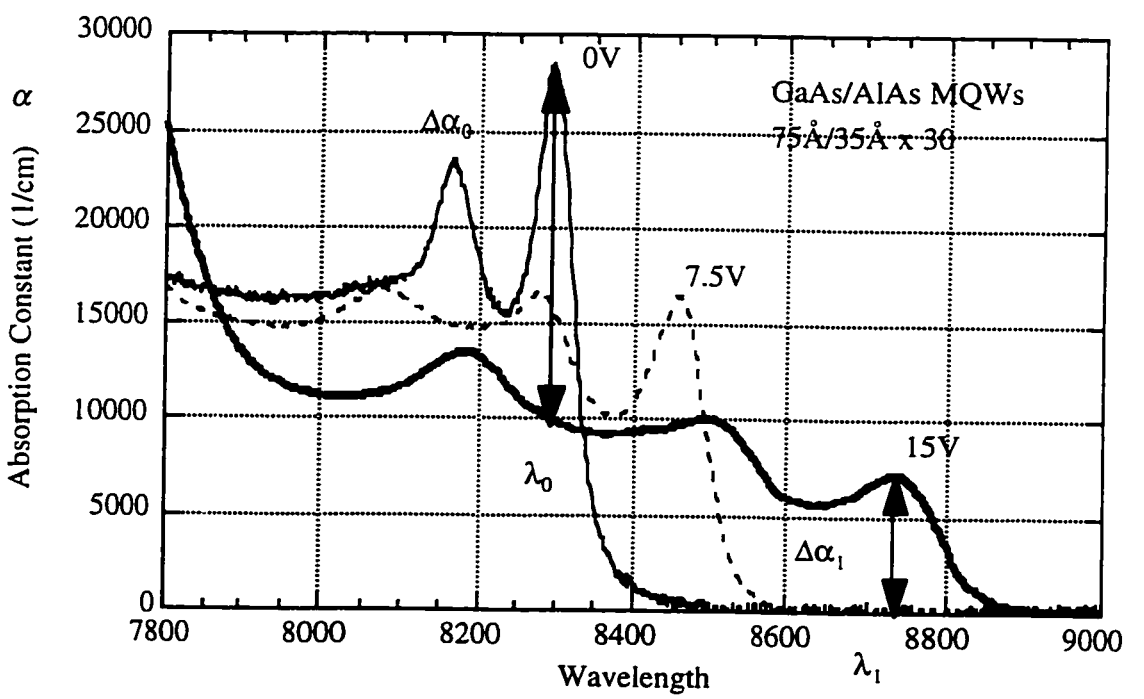

Figure 2.2. Absorption spectra of a GaAs/AlAs MQW structure under three different electric field levels.

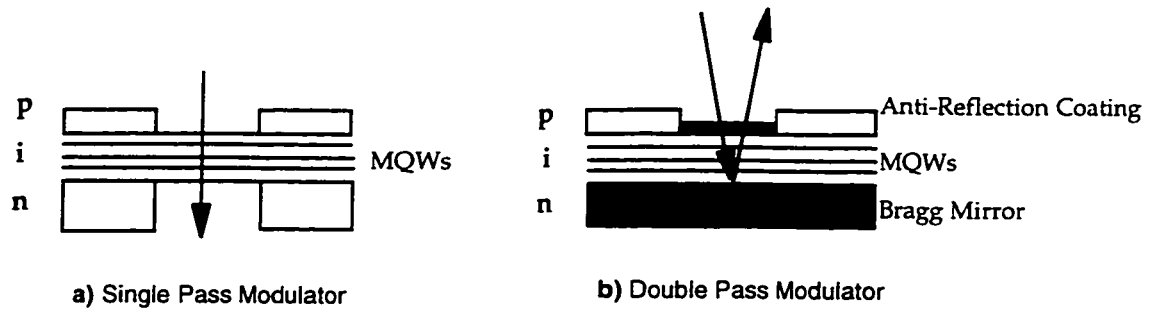

Figure 2.3 Structure of (a) a single pass modulator and (b) a double pass modulator

2.2 Fabry-Perot modulators

After the discovery of Quantum Confined Stark Effect (QCSE), Multiple Quantum Well (MQW) material was soon incorporated into a single pass structure to make a transmission modulator [24], as illustrated in Figure 2.3(a). The device was fabricated by removing part of the substrate to expose the MQW material and then coating both sides of the MQW with anti-reflection layers. The contrast ratio achieved from such a device was about 2 to 1, which is not high enough for many applications. The reason for the low contrast is that even though the QCSE is much stronger than the Franz-Keldish electro-absorption effect of bulk material, it still does not provide adequate absorption change to achieve high contrast ratio modulation in a single pass configuration. This could be improved with a thicker MQW region, but due to the limitations of material growth technology, growth of good single crystalline quality MQW material more than a couple of micrometers is difficult and very time consuming to grow. For example, with an absorption change of 5000 cm^{-1} and with a typical device thickness of 1μm , the contrast ratio for the transmission of light through a MQW layer is only 1 to 1.65, as given in the following equation,

$$\frac{I}{I_0} = \exp(-\Delta\alpha L) \approx \frac{1}{1.65} \tag{2.1}$$

To enhance the contrast ratio of the modulator, the path length of light through the active MQW material layer must be enhanced. One solution is to add a back mirror to the single pass device to make it into a double pass structure [25], as illustrated in Figure 2.3(b). An anti-reflection coating on the top surface was used in this design. The contrast ratio is improved by a factor of two over the single pass structure. Unfortunately this is still not satisfactory for many applications.

In 1989, it was proposed to place another mirror at the top surface such that the light can multiple pass between the mirrors in a Fabry-Perot interferometer[26] configuration. If the cavity is designed to have an optical thickness of integer multiple of $\lambda/2$, the optical field resonates inside the cavity and builds in intensity. Therefore, the QCSE can be enhanced more than in the double pass structure. This structure is a Fabry-Perot filter [27] with selective absorption inside the resonator according to applied electrical bias. Typically the mirrors are monolithically grown quarter wave stacks of two different semiconductor materials with different refractive indices. A typical structure is shown in Figure 2.4. The same structure is also used to make vertical cavity surface emitting lasers (VCSEL) [28,29]. Both the vertical cavity modulators and the VCSEL have similar advantages over conventional in-plane devices, such as, capability of dense two dimensional arrays, on wafer testing, and accurate control of the critical dimensions by epitaxial growth.

It is well known in spectroscopy that the reflection from a Fabry-Perot cavity has better contrast ratio than transmission. It results from impedance matching at the input of the device so that reflectance is zero at resonance, which is analogous to the impedance matching in electrical transmission lines. When the Fabry-Perot modulator is used in

reflection mode, under the correct matching condition, the cavity by itself provides the possibility of zero total reflectivity which is equivalent to an infinitely high contrast ratio.

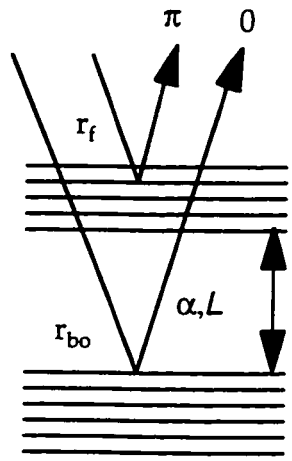

Figure 2.4 Phase relation between light reflections from a Fabry-Perot cavity.

Figure 2.4 illustrates the reflectance magnitude from a cavity structure. The light reflected from the top mirror has a phase change of 180° due to the half wave change from the air semiconductor interface, while the reflection from the bottom mirror does not have any phase change. With no absorption inside the cavity, the total reflectivity from this structure at the cavity resonance wavelength depends on the cancellation of these two contributions, which is given by [23]:

$$R = \left[\frac{r_b - r_f}{1 - r_b r_f}\right]^2 \tag{2.2}$$

in which r_b and r_f are the amplitude reflectivities of the front mirror and the back mirror respectively.

Equation (2.2) is only valid when there is no absorption inside the cavity, and under this condition, the total reflectivity is zero when the bottom and top mirror reflectivities are equal. This is called the impedance matching condition.

With absorption inside the cavity, the total reflectivity is given by [23]:

$$R = \left[\frac{r_b e^{-2\alpha L} - r_f}{1 - r_b r_f e^{-2\alpha L}} \right]^2 \tag{2.3}$$

in which α_e is the electric field absorption coefficient of the cavity, and L is the cavity length.

Equation (2.3) is essentially the same as equation (2.2) except that the back mirror reflectivity is now combined with the absorption inside the cavity to form a new effective back mirror reflectivity. This amplitude reflectivity is given by:

$$r_b^{eff} = r_b e^{-2\alpha_e L} \tag{2.4}$$

The corresponding intensity reflectivity is:

$$R_b^{eff} = R_b e^{-2\alpha L} \tag{2.5}$$

in which $\alpha = 2\alpha_e$, and $R_b = |r_b|^2$.

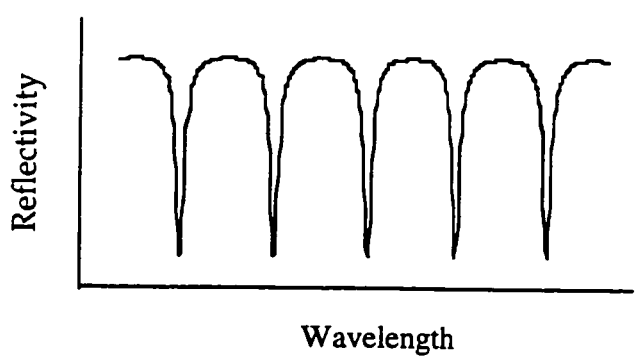

Figure 2.5. Reflectivity spectrum for a typical F-P cavity versus wavelength.

Now if the top mirror is designed to be a little less reflective than the bottom mirror and the absorption inside the cavity is adjusted by the QCSE in such a way that the

effective back mirror reflectivity can exactly match the front mirror reflectivity at a certain absorption level, then the impedance matching condition is achieved. When the cavity absorption is modulated between the low absorption condition and this matching condition, the total reflectivity of this device changes from a finite value to zero, which corresponds to an infinite contrast ratio. As a general rule, Fabry-Perot reflection modulators are designed with front mirrors set at lower reflectivities than those of the back mirrors to achieve a high contrast ratio [26,30,31].

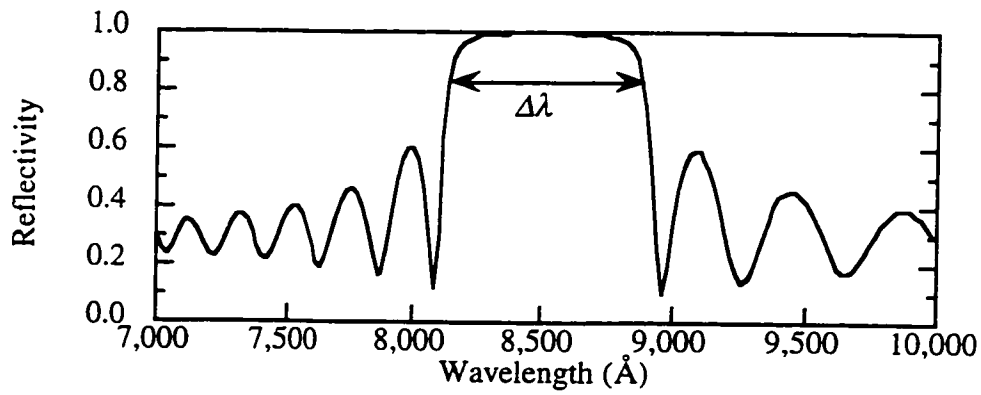

Figure 2.6 Reflectivity spectrum of quarterwave mirror stack

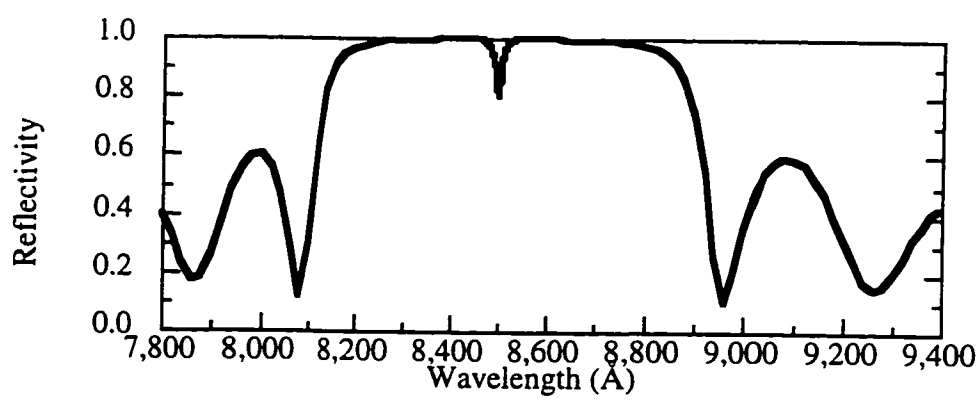

Figure 2.7 Typical reflectivity spectrum of a Fabry-Perot modulator

Figure 2.5 shows a typical reflectivity spectrum of a Fabry-Perot cavity with constant reflectivity mirrors versus wavelength. There are many characteristic reflectivity

dips correspond to resonance at each successive half wavelength. With vertical cavity semiconductor modulators, the mirrors are usually made with semiconductor quarter wave stacks. The reflectivity spectrum of such a stack is shown in Figure 2.6. There is a characteristic high reflectivity band around the designed wavelength of 850nm, indicated by $\Delta\lambda$ in the plot. Due to the limited refractive index contrast in the quarter wave stack material, this high reflectivity band is usually much narrower than the free spectral range between adjacent modes in a short vertical Fabry-Perot cavity. Therefore in a typical vertical cavity Fabry-Perot modulator, there is usually only one Fabry-Perot resonance in the high reflectivity band, shown as a small dip in reflectivity near 850nm in Figure 2.7, which is the reflectivity spectrum of a typical Fabry-Perot modulator with semiconductor quarter wave stack mirrors.

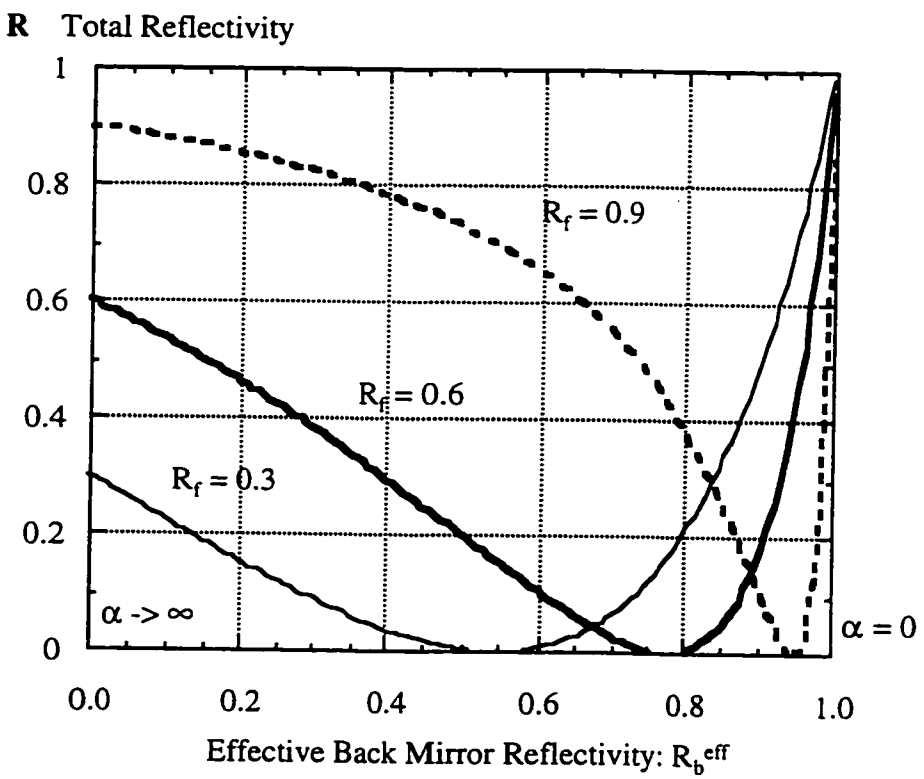

Figure 2.8. Total reflectivity as a function of effective back mirror reflectivity R_b^{eff}.

Figure 2.8 shows the total reflectivity versus the effective back mirror reflectivity, R_b^{eff}, as defined in equation (2.5) for three Fabry-Perot modulator designs with different front mirror reflectivities. It can be clearly seen that in the limit of zero absorption and the condition of a totally reflective (R = 1) back mirror, all incident light is reflected back no matter what the front mirror reflectivity is. On the other hand, if the absorption is infinitely high inside the cavity ($R_b = 0$), all light that passes through the front mirror is absorbed and the total reflectivity is equal to the front mirror reflectivity. Between these two limits, the reflectivity of the device is given by equation (2.2), and at cavity absorption level at which the effective back mirror reflectivity matches the front mirror reflectivity, the device reaches the matching condition which results in zero total reflectivity.

Figure 2.9 shows the structure of a typical Fabry-Perot reflection modulator: Electrically it is a p-i-n diode and optically it is a Fabry-Perot cavity with two doped quarter wave stack mirrors and an intrinsic MQW cavity. The mirrors consist of alternating high refractive index $Al_xGa_{1-x}As$ layer and low index AlAs layer, both of which are transparent around the operating wavelength. They are doped p type and n type respectively, and metal contacts to them are made with a window in the top contact to facilitate light input. The cavity is intrinsic MQW material with an optical thickness of integer multiple of $\lambda/2$. The whole structure was grown by Molecular Beam Epitaxy (MBE) on a doped GaAs substrate at a growth temperature of 600°C. The substrate rotation rate was set to 15rpm to ensure good uniformity across the wafer. In-situ growth rate monitoring and correction were utilized during the growth [32,33].

The major performance advantage of this kind of modulator is its high contrast ratio capability. Figure 2.10 shows the modulation spectra of this device under different levels of electric bias. The wavelength range from 820nm to 880nm is the high reflectivity band of the quarter wave stack mirrors, and near the center of this band is a cavity

resonance dip at around 846nm. At 0V bias, the absorption inside the cavity is low, and the total reflectivity is 90%, which is dominated by the back mirror reflectivity. As the electric field increases to 30V due to QCSE, the exciton absorption peak red shifts to about 835nm, as can be seen in the small dip to the left of the Fabry-Perot cavity dip in Figure 2.10. The reflectivity at the cavity resonance wavelength decreases down because of the increasing absorption inside the cavity. When the electric bias increases further to 37V, the exciton absorption peak red shifts even further to overlap with the cavity resonance wavelength. Because of the high absorption inside the cavity, the matching condition is reached and the total reflectivity decreases to almost zero.

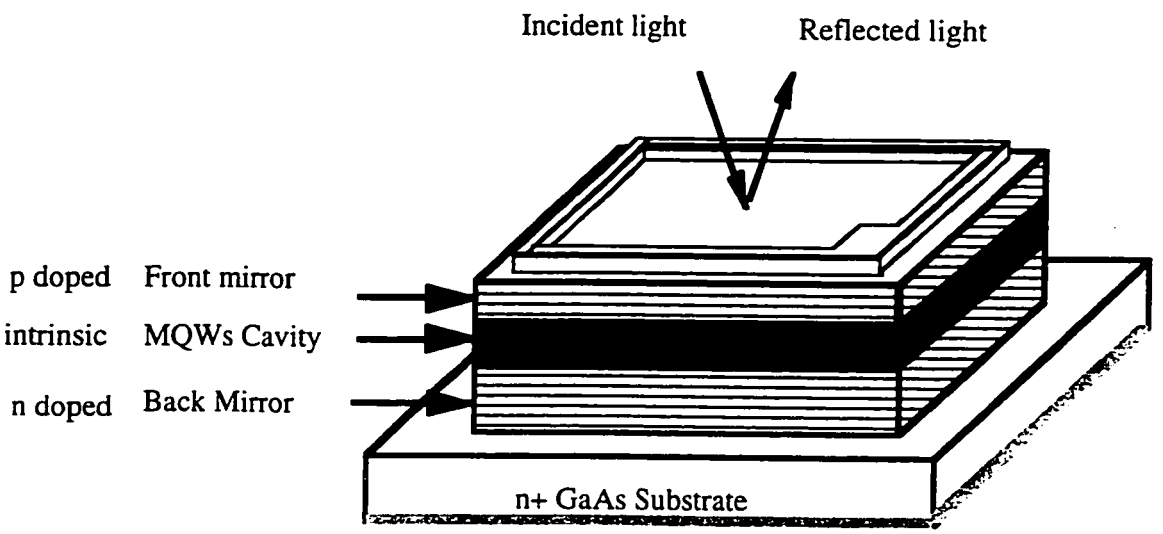

Figure 2.9. Structural diagram of a typical single cavity device

From the above example, it is clear that the Fabry-Perot reflection modulators have great potential in many applications due to their high contrast ratio capability. However, there are still some issues that need to be resolved before they can be utilized in real applications. The first issue is the phase properties of these modulators, which are very important for high speed optical communication applications since parasitic phase

modulation is a major barrier in limiting the bandwidth of communication systems based upon intensity modulation schemes.

The second issue is the optical bandwidth of these Fabry-Perot reflection modulators. In principle, a broad optical bandwidth modulator is more desirable for many applications. Unfortunately, in reality a narrow bandwidth in a Fabry-Perot modulator can be easily achieved by increasing the mirror reflectivities while a broad bandwidth is harder to achieve due to the conflicting limitations between cavity length and mirror reflectivity. New designs to broaden the optical bandwidth will be discussed in detail in chapter 5.

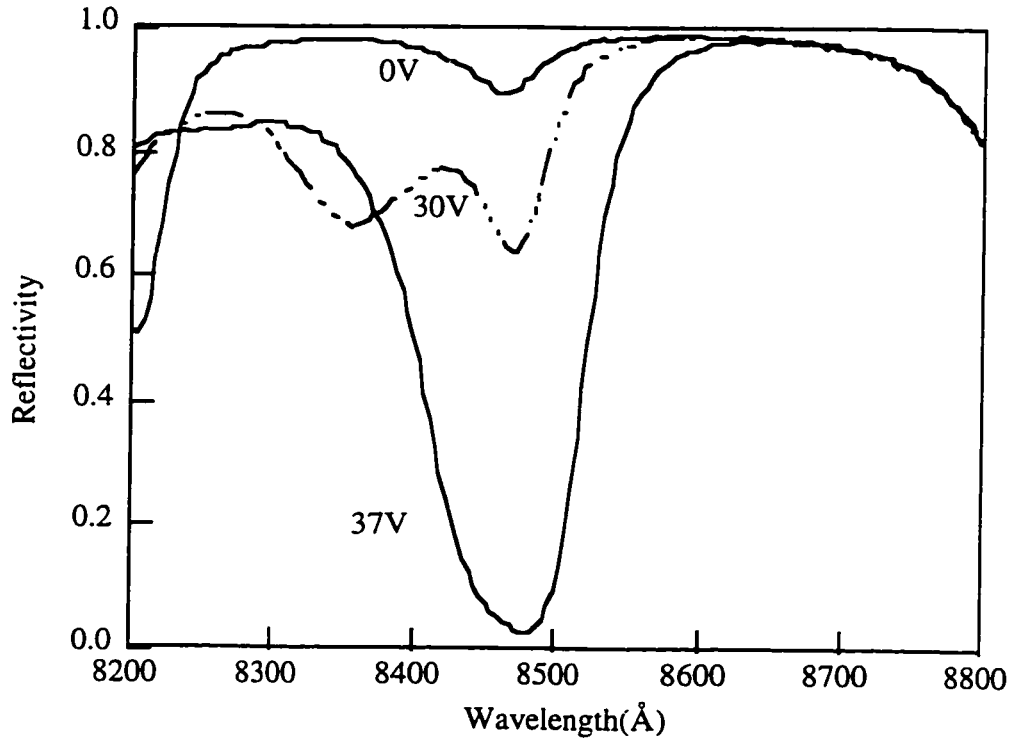

Figure 2.10. Reflectivity spectra of a Fabry-Perot modulator under three voltage bias conditions

2.3 Thin film simulation method

To provide guidance in the design process and to provide insight in analyzing the properties of Fabry-Perot modulators, a transfer matrix method [34] is utilized to simulate all the modulator devices. In fact this method can be applied to any layered structure with a non-absorbing substrate material. Figure 2.11 illustrates such a general structure:

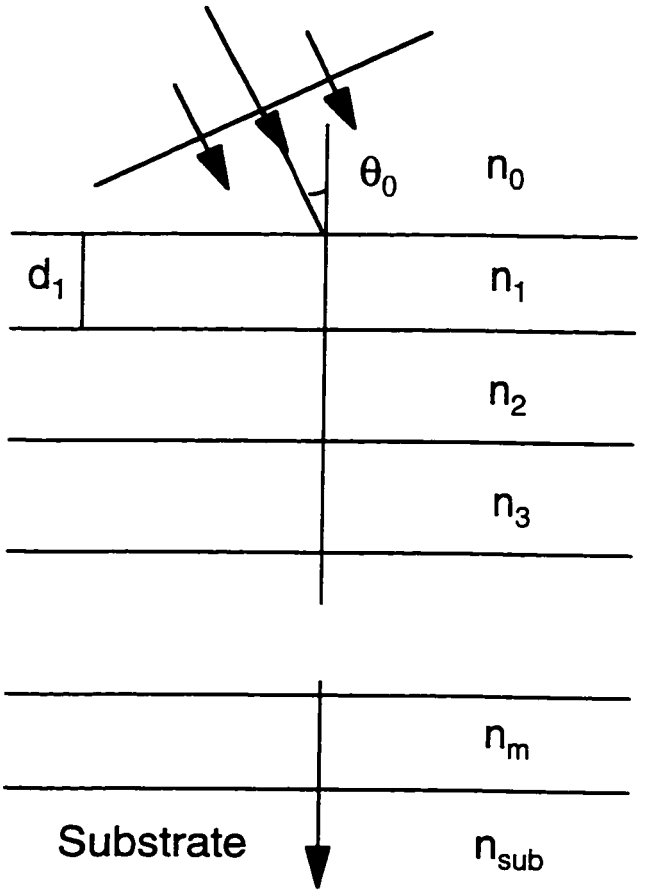

Figure 2.11 Diagram of a multilayer structure.

In this method each layer in the modulator structure is represented by a single 2x2 transfer matrix with the layer thickness and the corresponding complex reflective index as the parameters.

$$M_r = \begin{bmatrix} \cos\phi_r & (j\sin\phi_r)/\eta_r \\ j\,\eta_r \sin f_r & \cos\phi_r \end{bmatrix} \tag{2.6}$$

in which,

$$\phi_r = \frac{2\pi \tilde{n}_r d_r \cos\theta_r}{\lambda} \qquad \tilde{n}_r = n_r - jk_r \tag{2.7}$$

$$\eta_r = \begin{matrix} \tilde{n}_r \cos\theta_r \ \textit{for TE waves} \\ \tilde{n}_r / \cos\theta_r \ \textit{for TM waves} \end{matrix}$$

and n_r is the real part of the complex refractive index. k_r is the imaginary part of the complex refractive index. θ_r is the incident angle of light in the corresponding layer.

The total reflectivity and phase property of the whole structure can be derived by the multiplying product of all these matrices.

$$\begin{bmatrix} 1 \\ Y \end{bmatrix} \propto \begin{bmatrix} B \\ C \end{bmatrix} = \left\{ \prod_{n=1}^{m} M_r \right\} \begin{bmatrix} 1 \\ \eta_{m+1} \end{bmatrix} \tag{2.8}$$

The electric field reflectivity is given by:

$$r = \frac{\eta_0 - Y}{\eta_0 + Y} = \frac{\eta_0 B - C}{\eta_0 B + C} \tag{2.9}$$

in which η_0 is the optical admittance of the incident medium, which is:

$$\eta_0 = \begin{matrix} \tilde{n}_0 \cos\theta_0 \ \textit{for TE waves} \\ \tilde{n}_0 / \cos\theta_0 \ \textit{for TM waves} \end{matrix} \tag{2.10}$$

The total intensity reflectivity and transmissivity are:

$$R = \left| \frac{\eta_0 B - C}{\eta_0 B + C} \right|^2 \tag{2.11}$$

$$T = \frac{4\eta_{m+1}\eta_0}{\left|\eta_0 B + C\right|^2} \tag{2.12}$$

In this method, the refractive indices of pure material are available from the literature [35], while the refractive indices of quantum well material are determined from experimental data in a two step process. First, the absorption coefficient of a particular quantum well system is derived from the photocurrent measurement of a separately grown sample which is anti-reflection coated to avoid any cavity effect. Then the real part of the refractive index is calculated via the Kramers Kronig transformation [36],

$$\Delta n(\lambda_0) = \frac{c}{\pi} P \int_0^{\infty} \frac{\Delta\alpha(\lambda) d\lambda}{1 - (\lambda / \lambda_0)^2} \tag{2.13}$$

Both parts of the complex refractive index of GaAs are used as references [37,20] in calculating Δn and $\Delta\alpha$ in the above transformation. The resulting complex refractive index is then assigned to the well region of the quantum well structure. The barrier region of the quantum well structure is treated as bulk material, since no absorption occurs in that region. This simulation agrees very well with experimental results.

An implementation [38] of this method in C language was developed by a former student, Michael Larson, and was used for all the simulations in this work.

3 Phase Property of Fabry-Perot Modulator

3.1 Motivation

In a communication system [39,40], two commonly used information encoding schemes are intensity modulation and phase modulation. In either case, a pure effect, i.e. pure intensity modulation or pure phase modulation, works better than mixed effects. Under a pure intensity modulation, the optical amplitude is:

$$E(t) = E_0 \cos\left(\omega_0 t\right) \tag{3.1}$$

in which ω_0 is the carrier light frequency, and E_0 is the modulated amplitude which can be expressed as:

$$E_0 = E_m\left(1 + C_m \cos\left(\omega_m t\right)\right). \tag{3.2}$$

in which E_m and C_m are constants, and ω_m is the modulation frequency.

The total optical amplitude is thus:

$$E(t) = E_m\left[\cos(\omega_0 t) + \frac{C_m}{2}\cos\left((\omega_0 + \omega_m)t\right) + \frac{C_m}{2}\cos\left((\omega_0 - \omega_m)t\right)\right] \tag{3.3}$$

Figure 3.1(a) shows the power spectrum of light signal under pure intensity modulation. The modulating signal generates two side bands equally spaced on both sides of the carrier frequency. The spacing is the signal frequency ω_m.

Under pure phase modulation, the optical amplitude is given by:

$$E(t) = E_0\cos\left(\omega_0 t + \varphi(t)\right) \tag{3.4}$$

in which ω_0 is the carrier frequency, E_0 is a constant, and $\varphi(t)$ is the modulated phase:

$$\varphi(t) = \varphi_0 + \varphi_m\cos\left(\omega_m t\right) \tag{3.5}$$

in which φ_0 and φ_m are constants, and ω_m is the modulation frequency.

The total optical field can be expanded into an infinite series:

$$\begin{aligned} E(t) &= E_0\cos\left(\omega_0 t + \varphi_0 + \varphi_m\cos\left(\omega_m t\right)\right) \\ &= E_0\left(\cos(\omega_0 t + \varphi_0)\left[J_0(\varphi_m) + 2\sum_{k=1}^{\infty}(-1)^k J_{2k}(\varphi_m)\cos\left(2k\omega_m t\right) + \ldots\right]\right) \end{aligned} \tag{3.6}$$

in which J_0 and J_{2k} are Bessel functions.

The power spectrum of pure phase modulation is shown in Figure 3.1(b), in which there is an infinite series of signal side bands on both sides of the central carrier frequency. The spacing between each adjacent bands is the modulation frequency ω_m.

If there is a parasitic phase modulation accompanying a pure intensity modulation, the power spectrum becomes a mixture of those of pure intensity and pure phase

modulation cases, as shown in Figure 3.1 (c). The spectrum is broader than either of the pure intensity modulation and the pure phase modulation case. Another effect that is not shown in this graph is that the carrier light frequency, which is ω_0 at the center of the power spectrum in Figure 3.1, can also be shifted during the modulation process as a result of the parasitic phase modulation. This effect is called "Chirp" [41]. "Chirp" is very undesirable for real applications since it not only spreads the signal over a broader spectrum but also shifts the carrier signal wavelength and thus demands more allocation of optical bandwidth for one channel of communication.

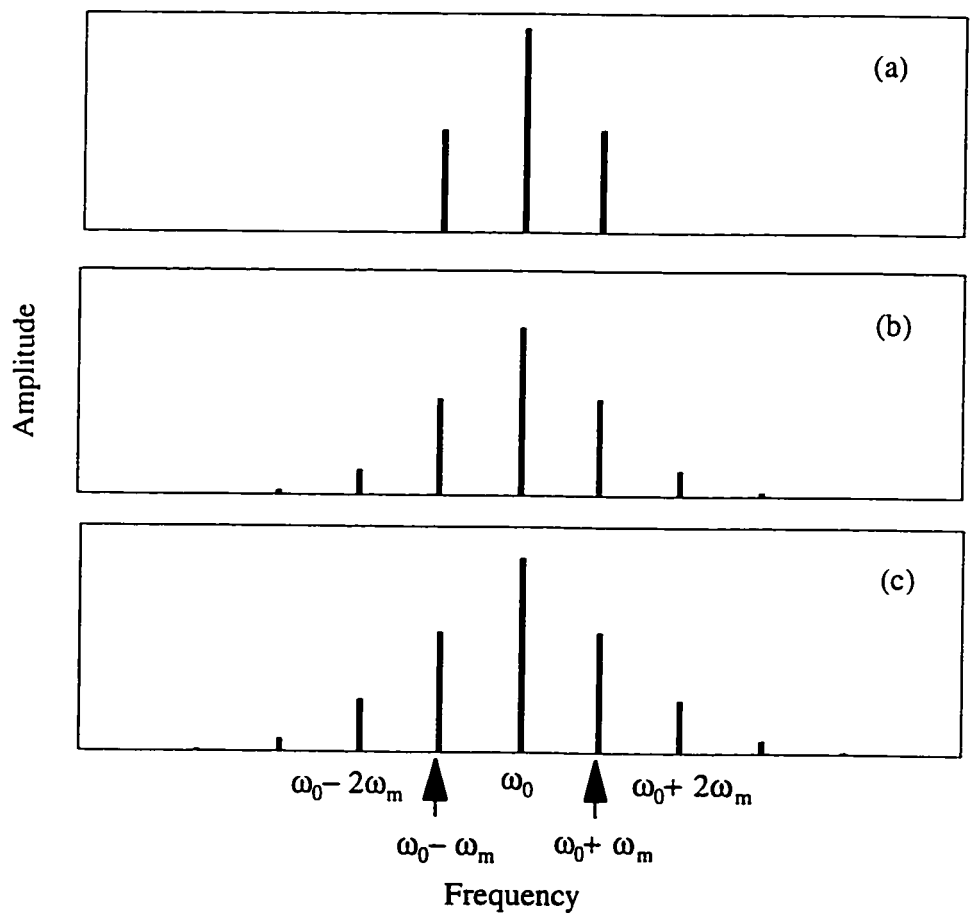

Figure 3.1 Power spectrum of light under (a) pure intensity modulation, (b) pure phase modulation, and (c) intensity modulation with parasitic phase modulation .

A commonly used parameter to describe the chirp effect is the chirp parameter, α_c.[41,42,43] It is defined as the ratio of the change in the real part and the change in the imaginary part of the complex refractive index.

$$\alpha_c \equiv \frac{\Delta n_{real}}{\Delta n_{imag}} \tag{3.7}$$

In a simple transmission modulator made from a slab of isotropic material, the output optical amplitude is:

$$E_{out} = E_{in} \exp\left(i\,(kL - \omega t)\right) \tag{3.8}$$

in which E_{in} and ω are the constant optical amplitude and the frequency of the input carrier light, respectively. L is the thickness of the transmission modulator, and k is the propagation constant inside the modulator:

$$k = \frac{2\pi}{\lambda}\left(n_{real} + i n_{imag}\right) \tag{3.9}$$

in which λ is the free space wavelength of the carrier light, n_{real} and n_{imag} are the real part and the imaginary part of the complex refractive index of the modulator material.

The intensity and phase of the output light through this transmission modulator are given by:

$$I_{out} = \left|E_{out}\right|^2 = I_{in} \exp\left(-\frac{4\pi n_{imag} L}{\lambda}\right) \tag{3.10}$$

and

$$\varphi_{out} = \frac{2\pi n_{real} L}{\lambda} \tag{3.11}$$

in which I_{in} is the constant input optical intensity.

If this simple transmission modulator is a pure intensity modulator, then from equations (3.10) and (3.11), only the imaginary part of the refractive index changes during the modulation process and therefore the chirp parameter is zero. Similarly in a pure phase modulator, only the real part of the refractive index changes and thus the chirp parameter is infinite. For a real device, the value of its chirp parameter is between these above two limits and it indicates how close this device is to either limit. For an intensity modulator, its chirp parameter should be as small as possible.

For semiconductor lasers, changes in refractive index is caused by fluctuation of the carrier density, N, during direct modulation of the injection current, and the chirp parameter [44,45] is defined as:

$$\alpha_c \equiv \frac{dn_{real} / dN}{dn_{imag} / dN} \tag{3.12}$$

which has a value between 2 and 7 [46]. For modulators, the chirp parameter is usually much lower [47,48] (around 1) because of the absence of majority carriers which are the main factor modulating the refractive index. Hence, there is an advantage in using an external modulator together with a laser running at a constant power level as compared to a directly modulated laser due to the lower parasitic phase modulation associated with the modulator.

3.2 Two factors determining the phase property of a Fabry-Perot modulator

The phase property of a Fabry-Perot modulator is affected by two factors: the refractive index change inside the cavity and the absorption change inside the cavity.

The refractive index change inside the cavity changes the optical thickness of the cavity, which shifts the cavity resonance wavelength and thus changes the reflection phase. This change of refractive index is determined by Kramers-Kronig relation [37,49,50] which links change of absorption constant with change of refractive index in any material system according to equation (3.3):

$$\Delta n(\lambda_0) = \frac{c}{\pi} P \int_0^{\infty} \frac{\Delta\alpha(\lambda) d\lambda}{1-(\lambda/\lambda_0)^2} \tag{3.13}$$

in which the integration is a principle value, i.e., the singularity point at λ_0 is excluded.

For quantum well material using the Quantum Confined Stark Effect, the absorption coefficient can be easily derived from a photo-current measurement [18]. Unfortunately, the value of the refractive index is very hard to measure due to the thinness of the available MQW material. To find this refractive index, one method [37] has commonly been used. There are three steps in this method. First, the absorption data of pure GaAs is used as a reference against the data of MQW material to calculate the difference in absorption. Next, equation (3.3) is applied to this difference of absorption which provides a difference in refractive index. Finally, the refractive index of pure GaAs is added to this difference in refractive index to derive the refractive index of the MQW material. It is noted that since the material structure and properties of the GaAs / $Al_xGa_{1-x}As$ system are very similar to pure GaAs, this procedure is well justified and most importantly, the results from this method

agree well with experimental results. In our simulations of modulator properties, we used this method to estimate the refractive index of the MQW material.

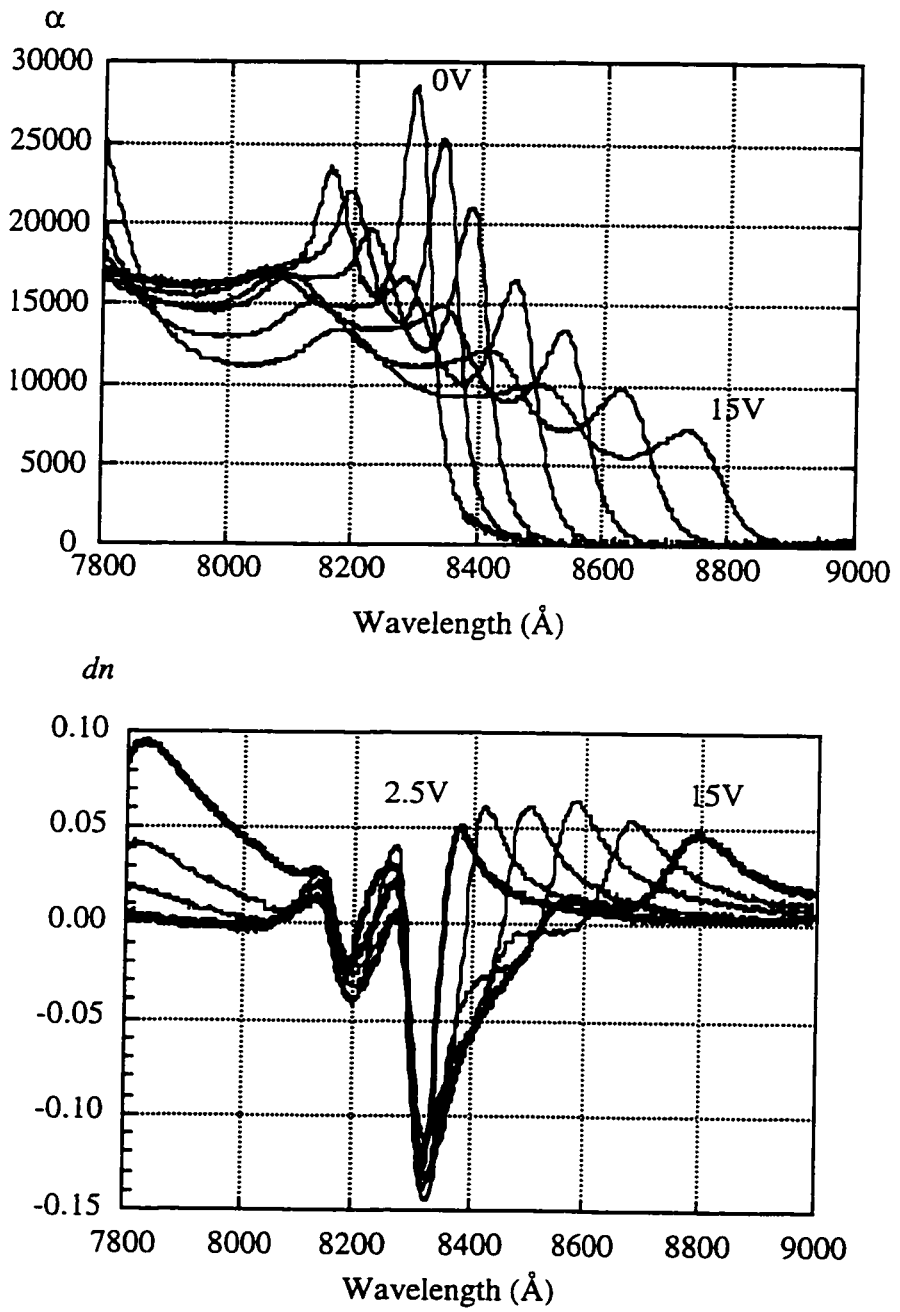

Figure 3.2 Refractive index change (bottom plot) as calculated from the absorption change (top plot) according to the Kramers-Kronig relation.

The change of refractive index can be very large in MQW. In Figure 3.2, the top plot shows the absorption spectra of a 75Å/35Å GaAs/AlAs Multiple Quantum Well system under seven different electric field levels, and the bottom plot shows the corresponding refractive index changes relative to the zero-field case as calculated from the Kramers-Kronig relation for the six non-zero electric field levels. The maximum change of refractive index is 0.14, which is quite large compared to the bulk effect. However, one drawback of this large refractive index change is that it is close to the wavelength of maximum absorption change, and for this reason it is not suitable for use as the modulating effect in a pure phase modulator.

The second factor that determines the phase property of a Fabry-Perot reflection modulator is the absorption change inside the cavity. Figure 3.3 shows two examples of how different absorption levels can affect the reflection phase. For Fabry-Perot modulators in general, the phase change associated with the top mirror is 180 degrees due to the half wave change at the air-semiconductor interface, and the phase change from the bottom mirror is zero degrees. Typically the bottom mirror is designed to be more reflective than the front mirror to achieve high contrast ratio. From equations (2.3) and (2.4), the total amplitude reflectivity of a Fabry-Perot reflection modulator at the cavity resonance wavelength can be expressed as:

$$r = \frac{r_b^{eff} - r_f}{1 - r_b^{eff} r_f} \tag{3.14}$$

in which $r_b^{eff} = r_b e^{-2\alpha_i L}$.

When the absorption inside the cavity is low, as illustrated in Figure 3.3(a), $r_b^{eff} > r_f$. As a result, r is positive, which means there is no phase change of the reflected light from the incident light. As illustrated in Figure 3.3(b), if the absorption inside the

cavity increases beyond the matching condition level (at which $r_b^{eff} = r_f$, resulting in zero total reflectivity), then the back mirror reflectivity r_b is attenuated by the absorption inside the cavity and the front mirror dominates the total reflectivity, i.e., $r_b^{eff} < r_f$. Now the value of r is negative, which means there is a phase change of 180 degrees between the reflected light and the incident light. So every time the absorption inside the cavity changes from below to above the matching condition level, $\alpha_e^{match} = \frac{1}{2L}\ln\left(\frac{r_b}{r_f}\right)$, the total reflection phase shifts 180 degrees.

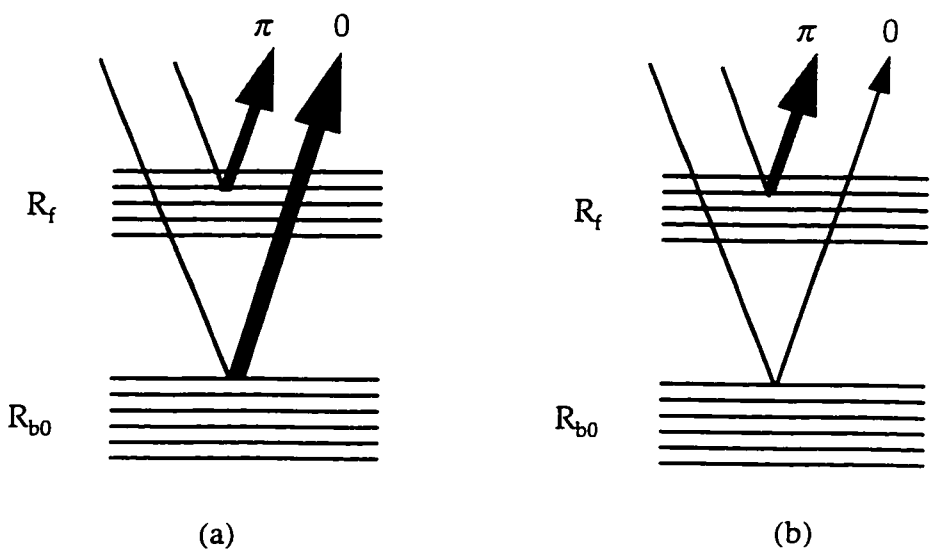

Figure 3.3 Absorption change inside the cavity alone can also lead to phase flip. (a) When α=0, back mirror dominates, phase of reflection is 0. (b) When α is large, front mirror dominates, phase of reflection is π.

Because of the above two contributing factors, the total reflected phase from a Fabry-Perot modulator is complicated. In order to achieve a better understanding of the phase properties of Fabry-Perot modulators and to help design better devices, an experimental method to accurately measure the phase change was needed. For this purpose,

we designed and modified an interferometer set-up [51] that enables us to accurately measure the phase characteristics of Fabry-Perot modulators.

3.3 Experimental phase measurement set-up

The modified Michelson interferometer setup [51] we designed and implemented to measure the phase characteristics of modulators is illustrated in Figure 3.4. The key feature of this setup is an electrically controlled movable mirror in one arm of the interferometer. The repetitive scanning of this mirror is the basis of the phase measurement.

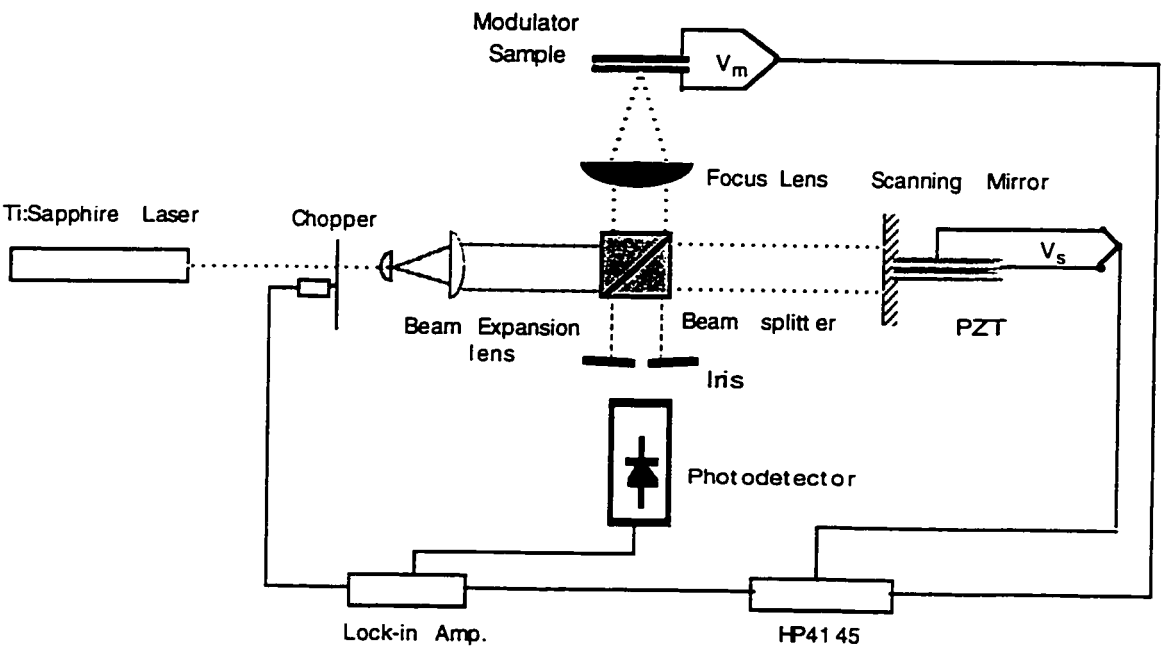

Figure 3.4 Schematic diagram of the experimental phase measurement set-up.

The light source in our setup is a tunable Ti:Sapphire laser. The wavelength is tuned to the point of interest within the operating wavelength range of the modulator under test. The laser output light is first expanded and collimated, and is then split into two arms of the interferometer by the beam splitter. In one arm of the interferometer, the light beam is

focused onto a Fabry-Perot modulator sample, which is electrically controlled by the modulation voltage V_m. In the other arm, the mirror mounted on a piezoelectric transducer is scanned back and forth to change the optical path length under the bias voltage, V_s. The reflected light beams from these two arms recombine on the output screen to form a typical interference ring pattern. A photodiode detector with a small aperture is used with a Lock-In amplifier to measure the optical intensity only at the center part of this ring pattern versus V_s, under different bias voltages, V_m., on the modulator sample.

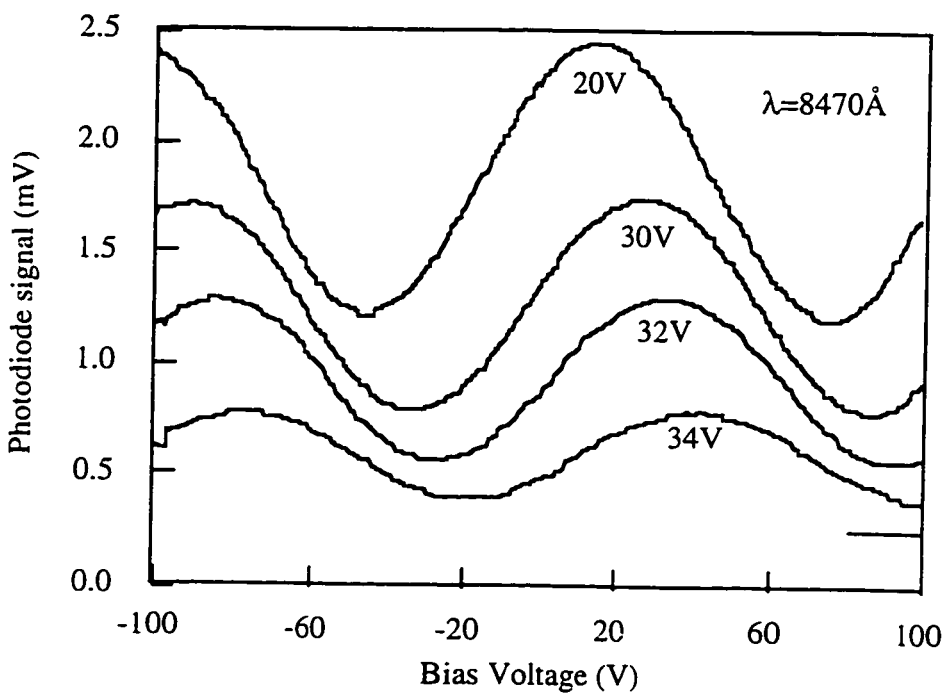

Figure 3.5 Phase measurement result for a Fabry-Perot modulator at four bias voltage levels on the modulator.

3.4 Operating principle of the phase measurement

An example of typical experimental results is shown in Figure 3.5. There are four sinusoidal curves corresponding to four different bias voltage levels on the modulator. We can clearly see three effects from the relationship between these curves: First, there are

phase shifts among them as seen from the different positions of the peaks and the valleys. Second, the DC levels, which represent the average optical intensity, change with modulator voltage. Third, the oscillation amplitude depends on modulator voltage, and here it decreases with increasing bias voltage.

The principle of operation for this phase measurement is explained by analyzing the interference intensity at the center of the ring pattern. At the photodetector aperture, the optical field amplitudes of reflections from the modulator and the scanning mirror (as shown in Figure 3.6) are expressed as:

$$E_1 = \beta E_0 r_m \exp\left(i\varphi_m\right) \tag{3.15}$$

$$E_2 = \beta E_0 r_R \exp\left(ik\,\Delta L + i\varphi_0\right) \tag{3.16}$$

in which φ_0 is the phase change from the scanning mirror, φ_m is the phase change from the modulator, r_m is the reflectivity of the modulator, r_R is the reflectivity of the movable mirror, k is the wave vector of the laser beam, ΔL is the change in distance from the movable mirror to the beam splitter, β is a common factor which includes the reflectivity of the beam splitter, and E_0 is the optical field amplitude of the incident light.

The total detected optical intensity at the center of the ring pattern is given by:

$$I = \left|E_1 + E_2\right|^2 = \beta^2 I_0\left(r_R^2 + r_m^2 + 2r_m r_R \cos\left(\varphi_m - \varphi_0 - k\,\Delta L\right)\right) \tag{3.17}$$

There are two parts in the above equation of the optical intensity. The first one is the DC part, which is the sum of the reflectivities of the modulator and the movable mirror. The second part is the AC part whose amplitude is proportional to the product of the reflectivities of the movable mirror and modulator. The frequency of the AC part is

determined by the scanning speed of the movable mirror; and the phase of the AC part is the phase difference between the modulator and the movable mirror. By comparing two intensity curves taken at different modulator voltage levels, the phase change of the modulator can be directly extracted.

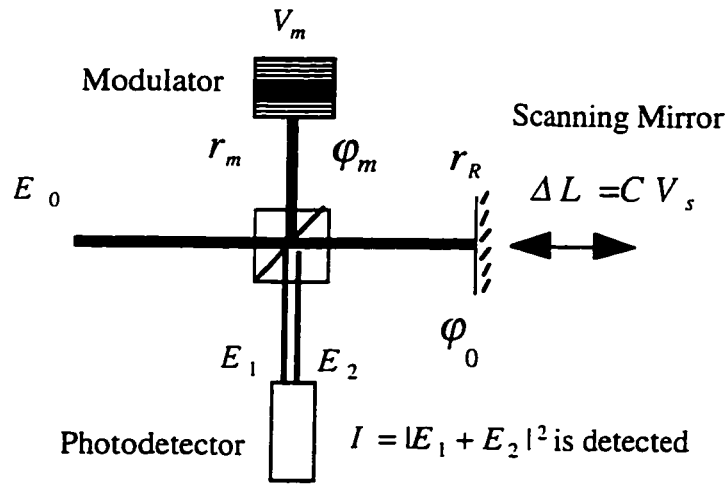

Figure 3.6 Illustration of the phase measurement principle.

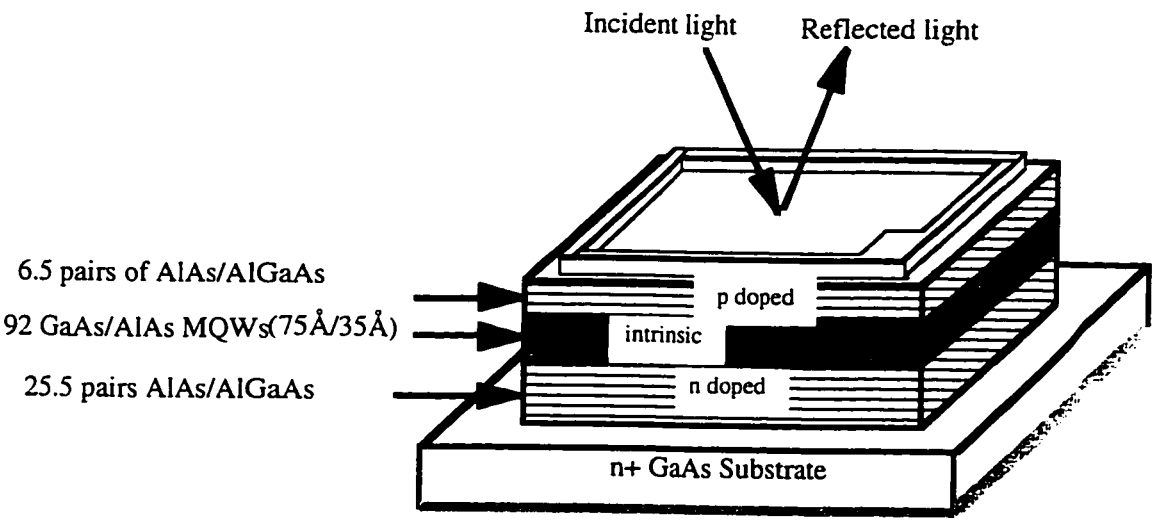

Figure 3.7 Structural diagram of the single cavity modulator used for phase measurement.

3.5 Results and discussion

We tested one modulator [52] in detail on this phase measurement set-up. It is a simple Fabry-Perot modulator with 6.5 pairs of AlAs/$Al_xGa_{1-x}As$ quarter wave stacks as the top mirror and 25.5 pairs of the same quarter wave stacks as the bottom mirror (Figure 3.7). The intrinsic cavity region consists of 92 GaAs/AlAs multiple quantum wells.

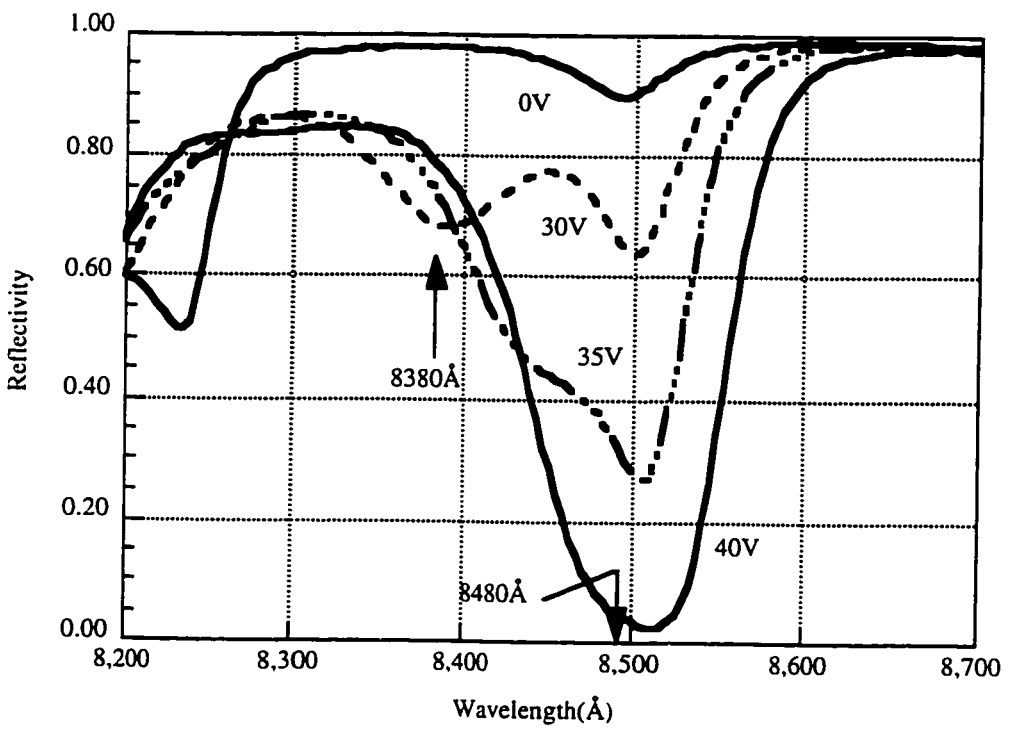

Figure 3.8 Reflectivity spectra of the modulator under test

Figure 3.8 plots the reflection spectra of this sample under different bias voltages. At 0V, there is a Fabry-Perot dip at 850nm, and the exciton peak is at 823nm. At 30V, a dip in reflectivity due to the shifted exciton peak is seen at 838nm. At 40V, this exciton peak red shifts further to 850nm, and the total reflectivity at this wavelength decreases to almost zero. Therefore this modulator has a very large reflectivity change at around 850nm.

Figure 3.9 shows the reflectivity change and the measured phase change versus bias voltage on the modulator at 838nm -- this is the wavelength of the exciton peak at 30V, well below the cavity resonance wavelength of 850nm. The reflectivity first decreases with increasing voltage, up to 32V; then increases gradually. The maximum change of reflectivity is about 20%. The measured phase change is very small, about 23 degrees. The general trend for the phase at this wavelength is that it decreases monotonically with increasing voltage level.

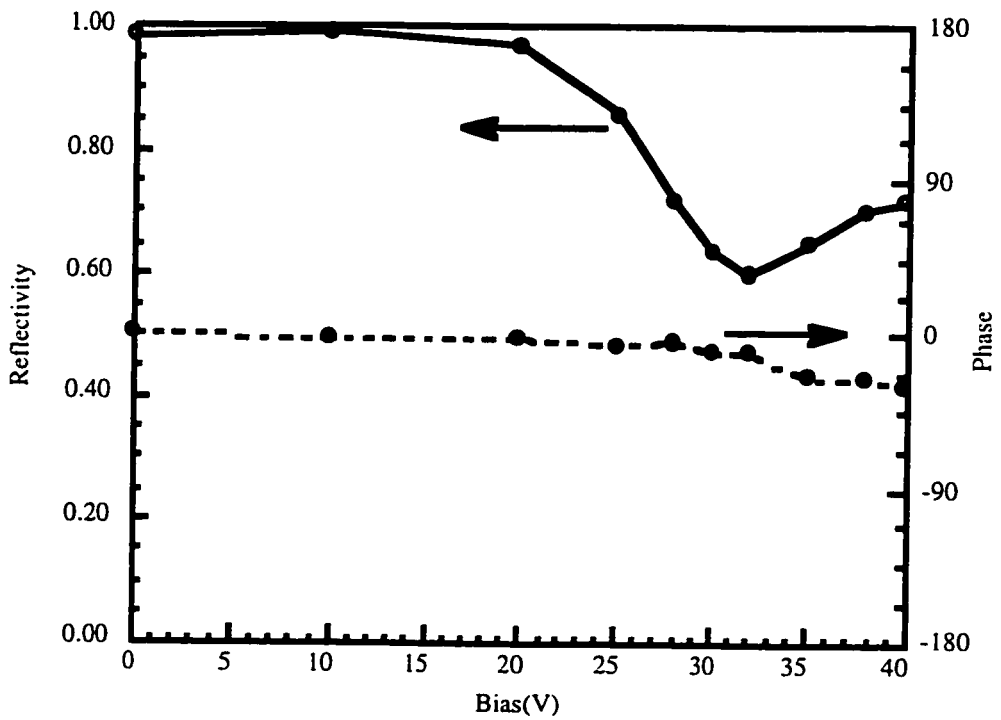

Figure 3.9 Reflectivity (left Y axis) and phase change (right Y axis) at 30V exciton peak wavelength (838nm).

Figure 3.10 shows the measured phase change and reflectivity of the tested modulator at the cavity resonance wavelength of 848nm. Here the reflectivity has a very large swing-- it decreases from 92% to almost 0% when the bias voltage increases from 0V to 38V, then the reflectivity increases slightly with increasing voltage caused by the

absorption going over the cavity matching condition. The phase change has a resonance behavior. With an increasing voltage, the phase of the modulator gradually decreases at first, then decreased at an accelerated rate until it reaches a minimum of -90 degrees at 35V, right before the reflectivity reaches its minimum. Above 35V, the phase change reverses its direction and starts to increase very sharply and reaches a maximum point of +140 degrees at 39V. Beyond 39V, the phase change starts to decrease gradually again. The maximum phase shift during the voltage scan is close to 240 degrees.

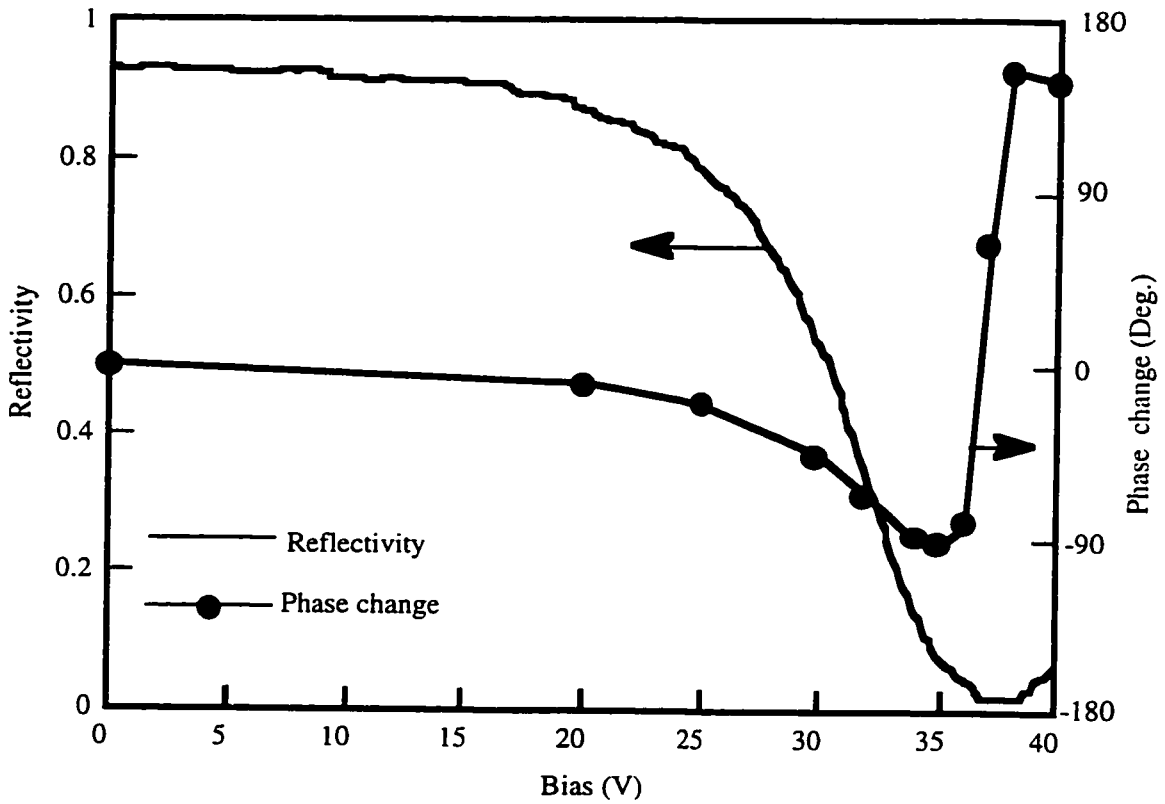

Figure 3.10 Reflectivity (left Y axis) and phase change (right Y axis) as a function of bias voltage at maximum contrast wavelength (8480Å)

To understand the complex phase characteristics of the tested modulator, we simulated our device with the thin film program [38]. Figure 3.11 and Figure 3.12 are the simulation results for the Fabry-Perot modulator . Since the chirp parameter of the MQW

material is neither reliable nor uniform, it is difficult to simulate the tested modulator with the empirical absorption data and the inferred refractive index data. We simplify the simulation by assuming that the cavity consists of uniform material in two cases of characteristic constant chirp parameters. The actual modulator has a chirp parameter that lies somewhere between the chirp parameters we chose.

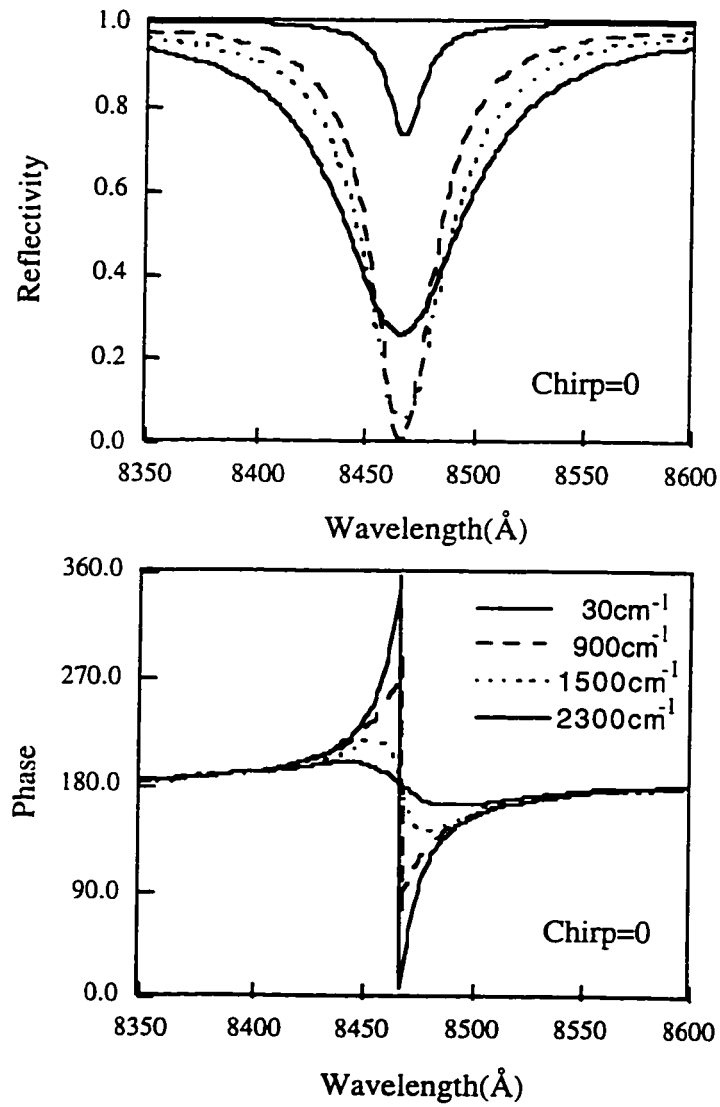

Figure 3.11. Simulation results of reflectivity and phase spectra of a Fabry-Perot modulator under four absorption levels inside the cavity. The chirp parameter $\alpha_c = 0$.

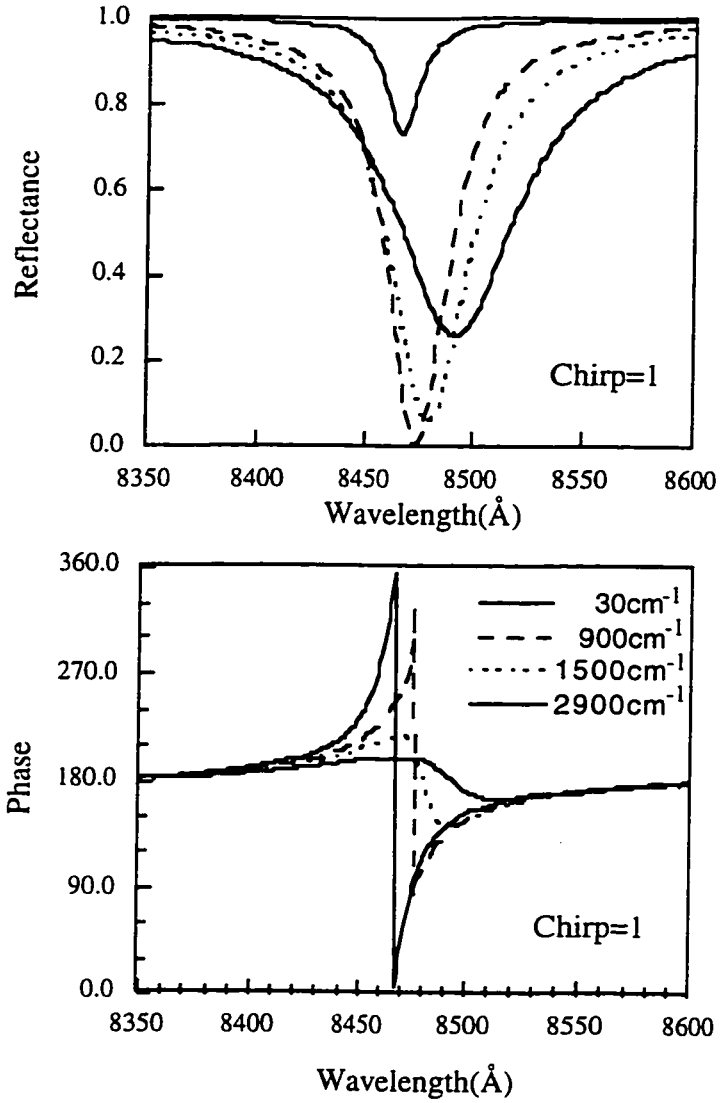

Figure 3.12. Simulation results of reflectivity and phase spectra of a Fabry-Perot modulator under four absorption levels inside the cavity. The chirp parameter $\alpha_c = 1$.

The two plots in Figure 3.11 show the reflectivity and phase spectra under different cavity absorption levels for a cavity material with zero chirp, i.e., there is no parasitic refractive index change when the absorption changes. From the top plot, it is clear that the reflectivity at the Fabry-Perot cavity resonant wavelength starts at a relatively high number(~80%) under low cavity absorption, and then decreases as the absorption inside

the cavity increases, until it reaches zero at the matching condition with an absorption of about 900 cm^{-1}. After the absorption level goes above the matching condition, the total reflectivity rises again but at a slower rate. As shown in the bottom plot of Figure 3.11, the phase of the reflected light at the resonant wavelength stays at zero degrees as the absorption increases and flips to 180 degrees when the absorption goes beyond the matching condition and does not change with further absorption increases.

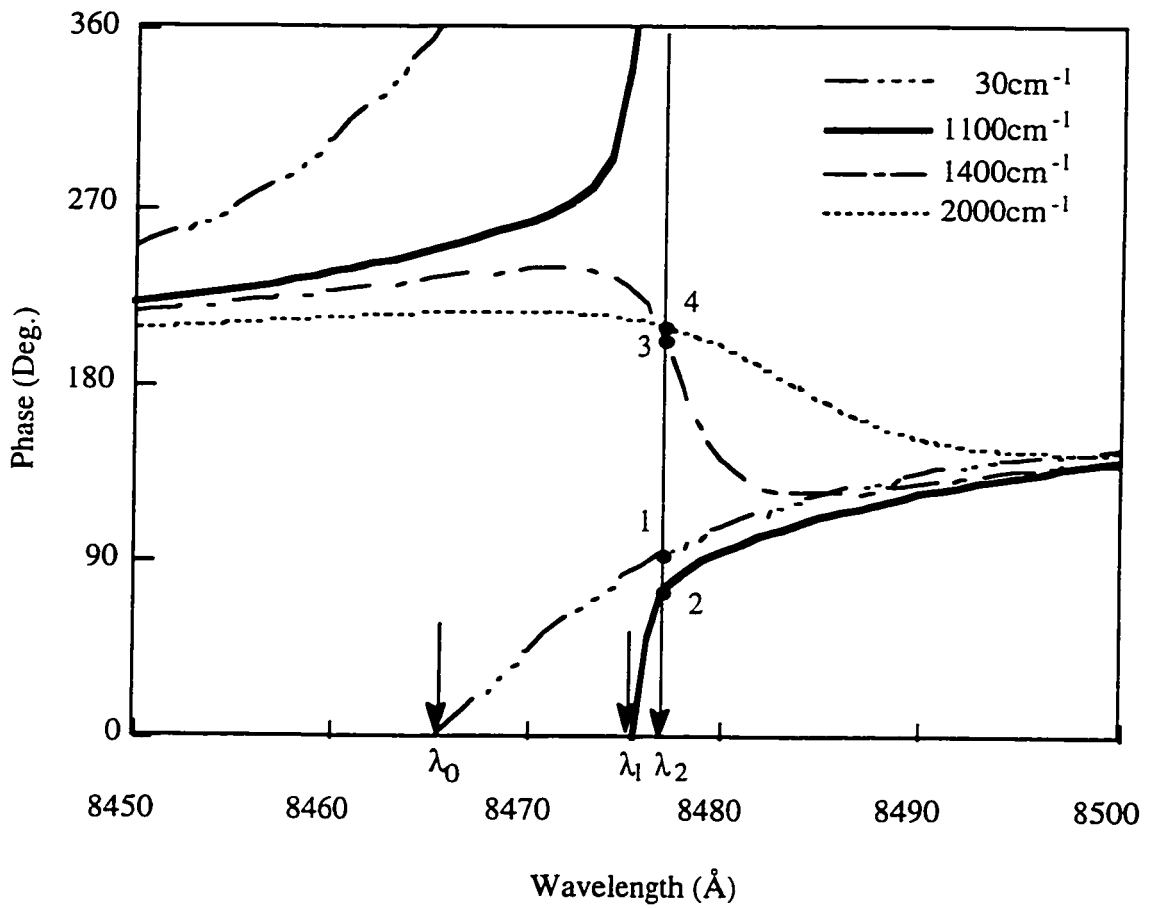

Figure 3.13. Simulated phase spectra of reflection from a Fabry-Perot modulator at different values of cavity absorption.

A phase flip modulator [52] can be constructed if we can operate this device between two specific absorption levels, for example, 300 cm^{-1} and 2300 cm^{-1}. The

reflection from this modulator will have the same reflectivity but opposite phase at these two absorption levels.

In reality MQW material does have a chirp parameter, which makes the phase behavior of the Fabry-Perot modulator more complicated. Shown in the two plots in Figure 3.12 are the reflectivity and phase spectra for a cavity with chirp parameter of one under the same set of absorption values as in the zero chirp case. Because of the chirp induced refractive index change, the cavity resonant wavelength is shifted to longer wavelength as the absorption level increases. The zero reflectivity wavelength is now at a wavelength longer than the original resonant wavelength. There is no clear point in wavelength where there is a 180 degree phase flip.

Figure 3.13 is a detailed view of the phase spectra for the $\alpha_c=1$ case. The absorption change inside the cavity affects the phase property directly by flipping the phase of reflection, especially near the resonant wavelength. It also affects the phase of reflection indirectly via the parasitic refractive index change.

Figure 3.14 includes three plots of reflectivity and phase versus absorption level inside the cavity at the three different wavelengths indicated in Figure 3.13. In Figure 3.14(a), the wavelength λ_0 is shorter than the cavity resonance wavelength. The reflectivity decreases gradually with increasing absorption but never goes to zero. This result agrees with our experimental results at 838nm.

Figure 3.14(b) is at the cavity resonance wavelength. The reflectivity goes to zero at an absorption level of 1200 cm^{-1}. The phase of the reflection has a large sharp drop of 200 degrees around the same absorption level. In Figure 3.14(c), the wavelength λ_2 is slightly longer than the resonance wavelength. The reflectivity still goes through zero, although at a higher absorption level of 1250 cm^{-1} . The phase of the reflection has a sharp

increase of around 100 degrees near the same absorption level. This last result agrees well with the experimental measurements at 848nm.

3.6 Summary

The reflection phase of a Fabry-Perot modulator is determined by both the absorption change inside the cavity and the refractive index change inside the cavity: The refractive index shifts the cavity resonant wavelength and this leads to a gradual shift of the reflection phase. The change of absorption inside the cavity can flip the reflection phase by 180 degrees at the resonant wavelength whenever the absorption crosses the matching condition. We designed and implemented a modified interferometer setup to accurately measure the phase properties of the Fabry-Perot modulator. We simulated the tested structure with a simplified model of uniform cavity material and the results agrees qualitatively with the experimental results. This phase measurement method has proven to be helpful in studies of both chirp free intensity modulators [53,54,55] and phase flip modulators [56,57].

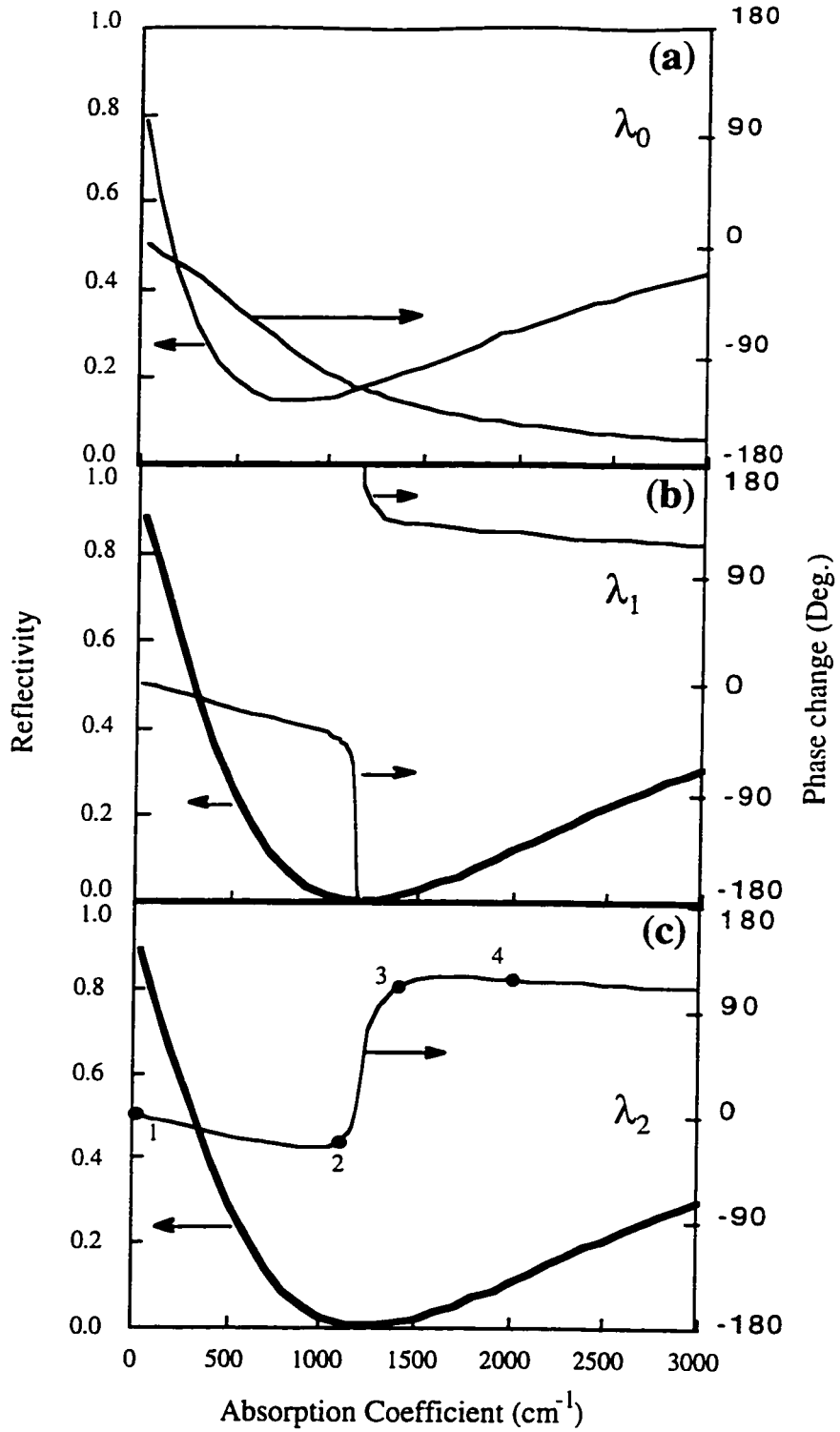

Figure 3.14. Simulation of reflectivity and phase change at three different wavelengths versus absorption levels for chirp = 1 case.

4 Short Cavity Fabry-Perot Modulator

4.1 Motivation

The optical bandwidth of a Fabry-Perot modulator [58,59] is an important performance parameter. It indicates the working wavelength range of either high contrast ratio or high reflectivity change. In general, a broad bandwidth is more desirable for two reasons: First, the design and growth tolerance of Fabry-Perot modulators are improved due to less stringent requirements of aligning the exciton peak absorption wavelength with the Fabry-Perot cavity mode wavelength. Second, in applications in which modulators are utilized to modulate narrow linewidth light sources, such as semiconductor lasers, broad bandwidth modulators improve both the manufacturing tolerance of the combined device system and the operational reliability of the system against either environmental (temperature, etc.) or other (power supply) fluctuations.

4.2 Optical bandwidth of a Fabry-Perot modulator

Depending on the application, there are many definitions of the optical bandwidth of a Fabry-Perot modulator. In this study, the optical bandwidth is defined as the full-width-

half-maximum (FWHM) wavelength range of the Fabry-Perot cavity dip in the reflectivity spectrum.

To illustrate the contributing factors to the optical bandwidth of a Fabry-Perot modulator, we first consider a simplified model, in which, to first order, a Fabry-Perot modulator is approximated as a simple uniform cavity sandwiched between two uniform mirrors. A uniform cavity means a cavity that is composed of one kind of pure material, such as GaAs. Uniform mirrors are mirrors of zero thickness and zero dispersion. In such a simple Fabry-Perot cavity structure, there are two major factors that determine the bandwidth. The first factor is the cavity length, which is inversely proportional to the optical bandwidth. The second factor is the reflectivity of the mirrors. In general, more reflective mirrors generate a higher cavity quality factor Q which leads to a narrower optical bandwidth.

Ideally a Fabry-Perot modulator should have a cavity with the minimum optical thickness of $\lambda/2$ if there is enough absorption change inside the cavity. This very short cavity length provides maximum optical bandwidth while still satisfying the phase requirement of a Fabry-Perot cavity. However, a $\lambda/2$ cavity is usually not adequate in practice due to the insufficient absorption change from the QCSE of the MQW material in the cavity. Even though the maximum absorption change from the QCSE is much larger than that from bulk material, it is still far from the level required for the matching condition between a 30% reflectivity front mirror and a perfect back mirror in a $\lambda/2$ cavity (about 120nm in length). To compensate for the short cavity length in a $\lambda/2$ cavity modulator, the front mirror reflectivity must be increased to make the light bounce several times before it escapes from the cavity. However, this increase in mirror reflectivity decreases the optical bandwidth of the modulator.

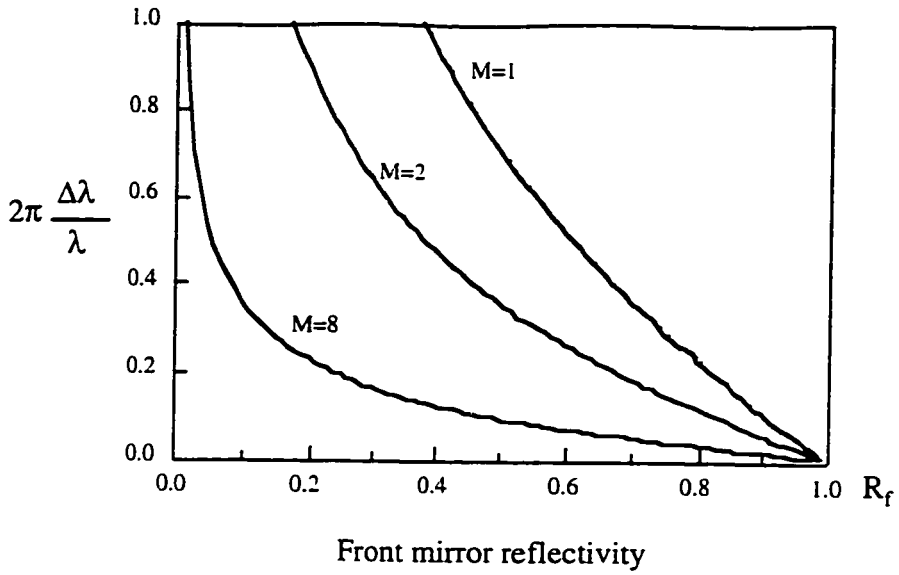

Figure 4.1 Bandwidth of three Fabry-Perot modulators with cavity optical thickness of $\lambda/2$ (M=1), λ (M=2), and 4λ (M=8) as a function of their front mirror reflectivities.

The effects of cavity length and mirror reflectivity on cavity bandwidth are illustrated in Figure 4.1, in which the full-width-half-maximum (FWHM) bandwidth of three simple Fabry-Perot cavities with different cavity lengths are shown as a function of the front mirror reflectivity. The back mirror has perfect reflectivity, which is the ideal case for reflection modulators. For all three cavity lengths, the bandwidth decreases with increasing front mirror reflectivity. Greater change of bandwidth occurs in the lower range of front mirror reflectivity, while the bandwidth does not change very much when the front mirror reflectivity is high. Comparing the three curves representing different cavity lengths, we can see that with the same front mirror, a Fabry-Perot modulator with a shorter cavity always has a greater bandwidth than the one with a longer cavity. To achieve broad bandwidth, both short cavity and low front mirror reflectivity are needed.

4.3 $\lambda/2$ short cavity modulator

As discussed above, cavity length must be as short as possible to insure a broad bandwidth for a Fabry-Perot modulator, but the maximum available absorption limits the

minimum cavity length at certain mirror reflectivities. We tried to solve this problem by breaking away from the conventional design of Fabry-Perot modulators, which presumes that the MQW material is only inside the cavity. In our new design, the active MQW material is put into the back mirror region and the cavity region is left free of MQW. Because the cavity is inactive in this design, its length can be designed to be as short as possible. One such design [60] is shown in Figure 4.2.

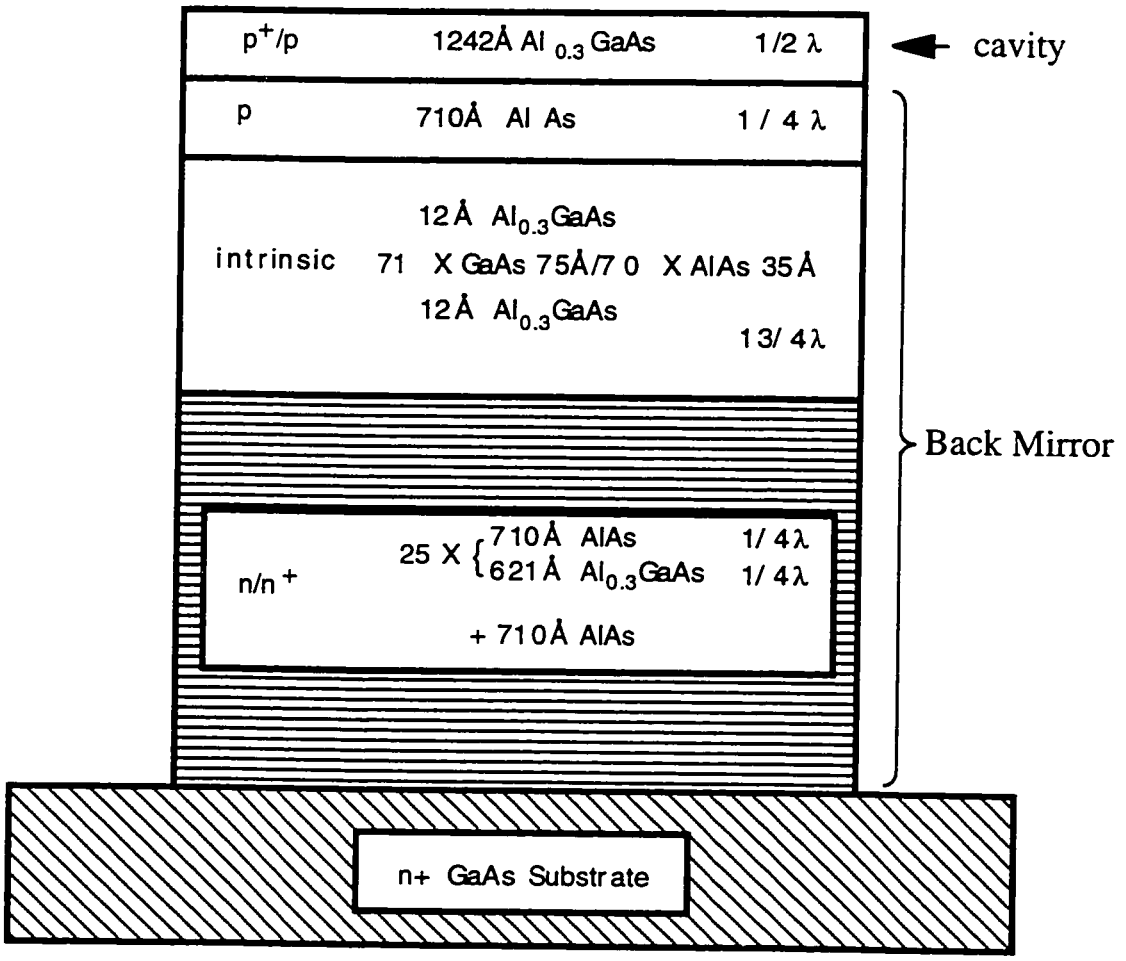

Figure 4.2. Structural diagram of a short cavity modulator with λ/2 cavity length.

In this design, a single λ/2 layer of inactive $Al_{0.3}Ga_{0.7}As$ material is the Fabry-Perot cavity, and a layer of 71 periods of active 75Å/35Å GaAs/AlAs MQW is

incorporated in the back mirror, which has another 25 periods of 710Å/621Å AlAs/ $Al_{0.3}Ga_{0.7}As$ quarter wave stacks. The main feature of this design is that the MQW layer has an optical thickness of 13λ/4, which is equivalent to a λ/4 high refractive index layer in terms of the phase condition. Since the MQW layer is part of the back mirror, the cavity of inactive $Al_xGa_{1-x}As$ can be readily optimized. We call this design λ/2 cavity modulator.

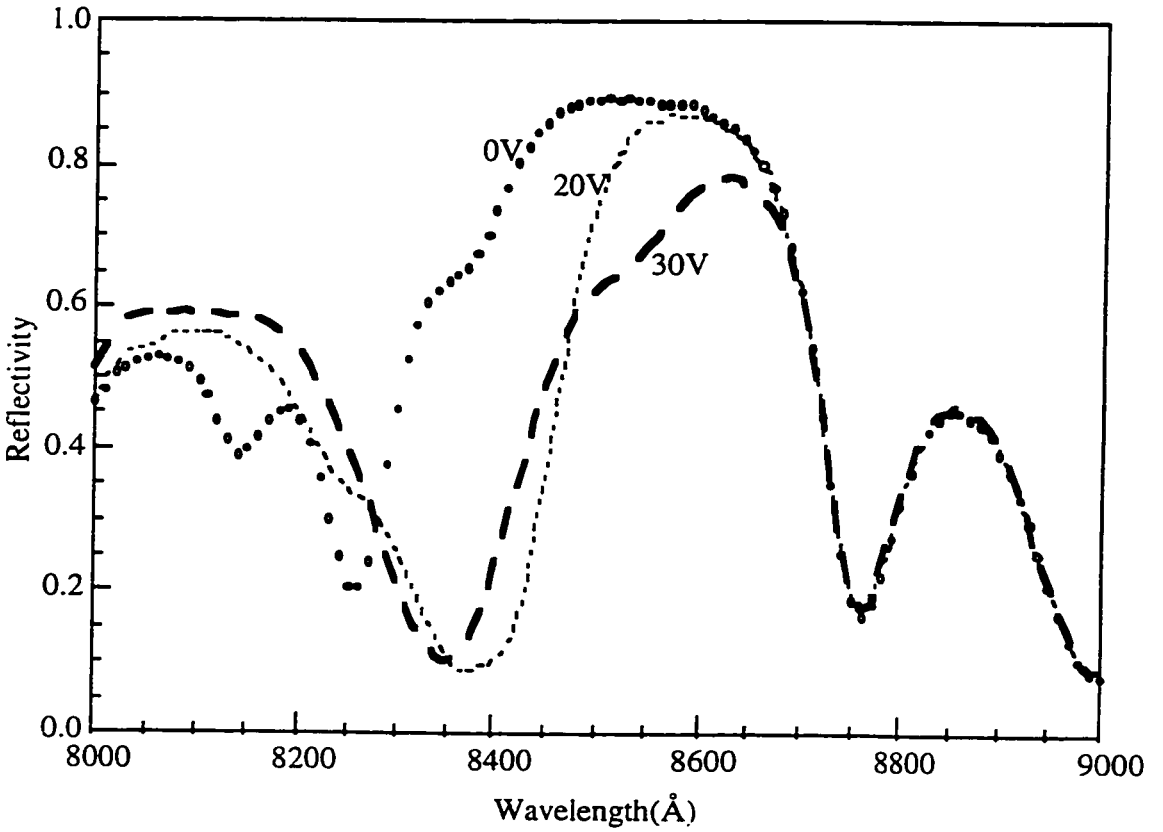

Figure 4.3 Reflectivity spectra of a short cavity modulator with λ/2 cavity

The measured reflectivity spectra of this λ/2 cavity modulator is shown in Figure 4.3. In the 0V curve, the Fabry-Perot dip is at 838nm and the heavy hole exciton absorption peak is at 826nm. As the bias voltage increases to 20V, the heavy hole exciton peak shifts to overlap with the Fabry-Perot cavity resonance wavelength. Maximum

modulation is about 70% reflectivity change at 840nm. The modulation bandwidth of this modulator is 15nm, which is about 10% broader than a conventional Fabry-Perot modulator with a MQW cavity of the same thickness.

We have demonstrated that this design indeed improves the bandwidth of a Fabry-Perot modulator. Unfortunately, the increase of 10% in bandwidth is not really significant for most practical applications. In order to expand the bandwidth of Fabry-Perot modulators, we explored several other short cavity designs which are described in the following sections.

4.4 Anti-reflection short cavity modulator

An alternative short cavity design is to incorporate the MQW in the back mirror and to use a special anti-reflection layer as the top cavity [61,62]. The refractive index value of this layer is chose to be in the middle of the refractive index value of the layer on top and the value of the refractive index of the layer below. The optical thickness of this layer is designed to be an odd integer multiple of $\lambda/4$. Due to these two characteristics, this layer is optically quite similar to an anti-reflection coating commonly used in conventional optics. One difference between this layer and a perfect anti-reflection coating layer is that the refractive index of this layer is not matched to those of the surrounding layers. This modulator design is referred as an anti-reflection(AR) modulator.

The equivalence [63] between such an anti-reflection cavity and a conventional Fabry-Perot cavity is demonstrated in Figure 4.4, in which the round trip phase conditions of light traveling inside these two cavities are compared. The round trip phase change within a layer of material is the sum of the phase change at the two surfaces of the layer and the phase change caused by the optical thickness of the layer. In the case of a Fabry-Perot cavity, which is designed to have a higher refractive index than those of the surrounding

layers, the phase changes of light reflection on both interfaces are zero, while the optical thickness of the cavity is:

$$n_{high}\, d = m\,\frac{\lambda}{2}\,. \tag{4.1}$$

in which n_{high} is the refractive index of the cavity, d is the length of the cavity, m is an integer, and λ is the resonant wavelength of the cavity. The total round trip phase change for a Fabry-Perot cavity is:

$$\Phi = \frac{2\pi}{\lambda} n_{high}\, 2d + 0 + 0 = 2m\pi \tag{4.2}$$

Since the refractive index value of the AR cavity is between those of the top and bottom layers, there is a phase change of π at the bottom interface and a phase change of zero at the top interface. However, the optical thickness of the cavity is:

$$n_{med}\, d = (2\,m - 1)\,\frac{\lambda}{2} \tag{4.3}$$

in which n_{med} is the refractive index of the cavity. The total round trip phase change is:

$$\Phi = \frac{2\pi}{\lambda} n_{med}\, 2d + \pi + 0 = 2m\pi\,. \tag{4.4}$$

Since this phase condition is the same as in a Fabry-Perot cavity, the AR cavity is equivalent to a Fabry-Perot cavity.

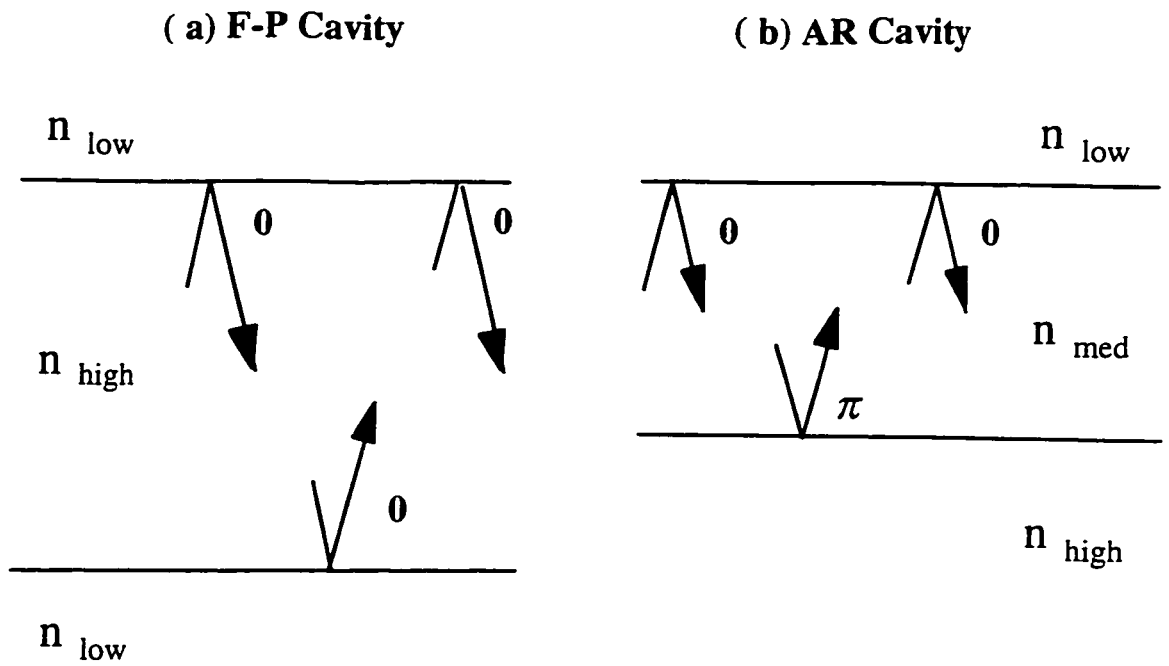

Figure 4.4 Comparison of two cavity structures: a) λ/2 cavity, and b) anti-reflection cavity. n_{high}, n_{med}, and n_{low} are refractive indices. $n_{high} > n_{med} > n_{low}$

When compared with conventional Fabry-Perot modulators, this anti-reflection cavity design has the same advantages as the λ/2 short cavity modulators due to its short cavity length. In addition, this anti-reflection design is better than the λ/2 short cavity design in two aspects. First, it reduces the cavity thickness further to a minimum of λ/4, which yields a even wider bandwidth than a λ/2 cavity. Second, in this design, the low refractive index λ/4 layer below the Fabry-Perot cavity in the λ/2 design is absent, and as a result, the optical field inside the MQW region of the back mirror is enhanced, which improves modulation efficiency.

Shown in Figure 4.5 is the schematic diagram of the structure of an anti reflection modulator [60]. It has a p doped 3λ/4 $Al_{0.4}Ga_{0.6}As$ layer as the top anti-reflection cavity. The

reason to adopt a $3\lambda/4$ cavity is that it is more tolerant of growth error (we can always etch back this layer after the MBE growth) and it helps in protecting the MQW region against p-type dopant diffusion. Also in this modulator, an intrinsic 71 period GaAs /AlAs MQW layer is sandwiched by the top p doped AR cavity and 15 pairs of n doped 710Å/621Å AlAs/$Al_{0.3}$GaAs quarter wave stacks. Since the optical thickness of the MQW layer is $13\lambda/4$, it joins the AlAs/$Al_{0.3}Ga_{0.7}As$ quarter wave stacks to form a back mirror. The top mirror is just the air semiconductor interface of the anti-reflection layer.

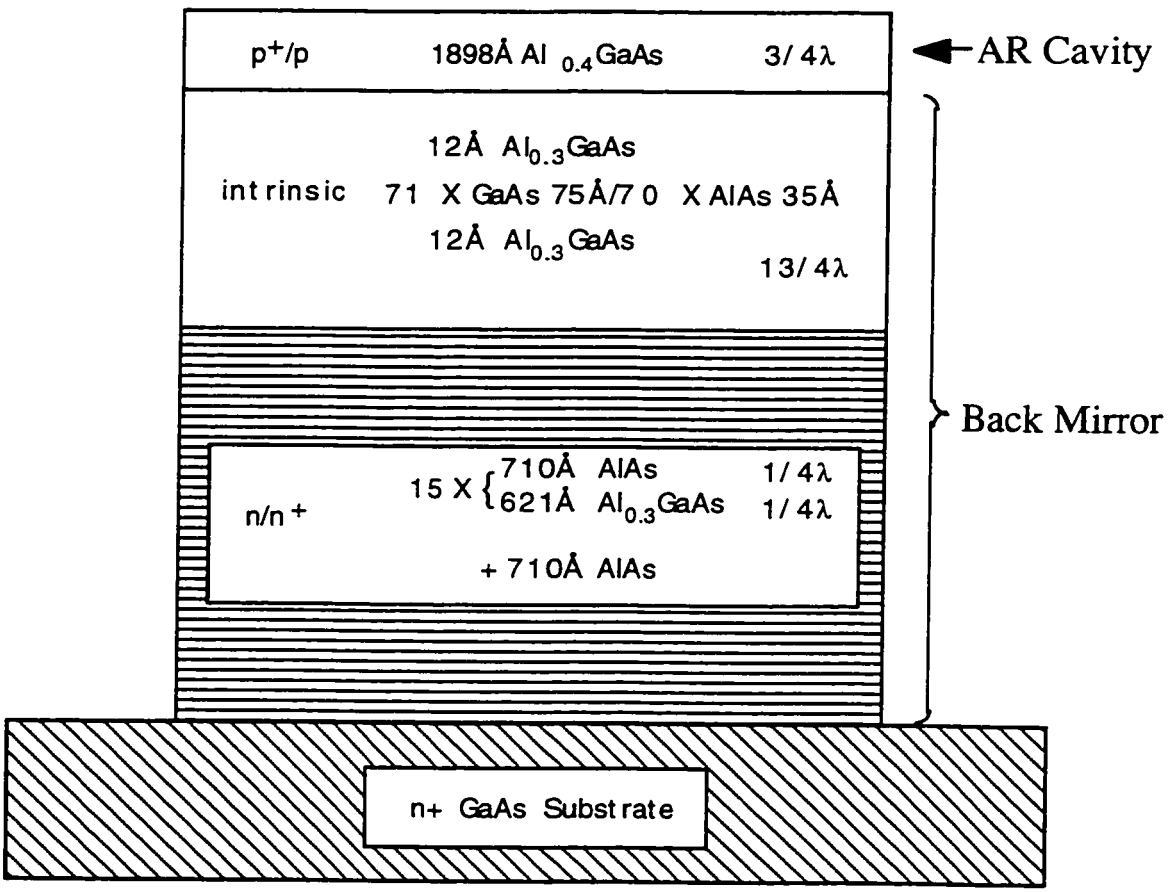

Figure 4.5 Device structure of a antireflection cavity modulator

The measured reflection spectra of this anti-reflection modulator is shown in Fig. 4.6. The Fabry-Perot dip at 848nm and the exciton absorption peak (825nm at 0V, 838nm

at 20V, and 848nm at 26V) are all present in the spectra curves. When the electrical bias is increased from 0V to 30V, the exciton absorption peak red shifts into the cavity resonance wavelength and total reflectivity is driven down to close to zero. The measured bandwidth of this device is 16nm which is about 7% broader than the $\lambda/2$ cavity modulator. However, the bandwidth improvement over a conventional Fabry-Perot modulator is not as pronounced as predicted by the simple model. Further detailed simulation has shown that reducing the cavity optical thickness from $3\lambda/4$ to $\lambda/4$ does not improve the modulation bandwidth very much.

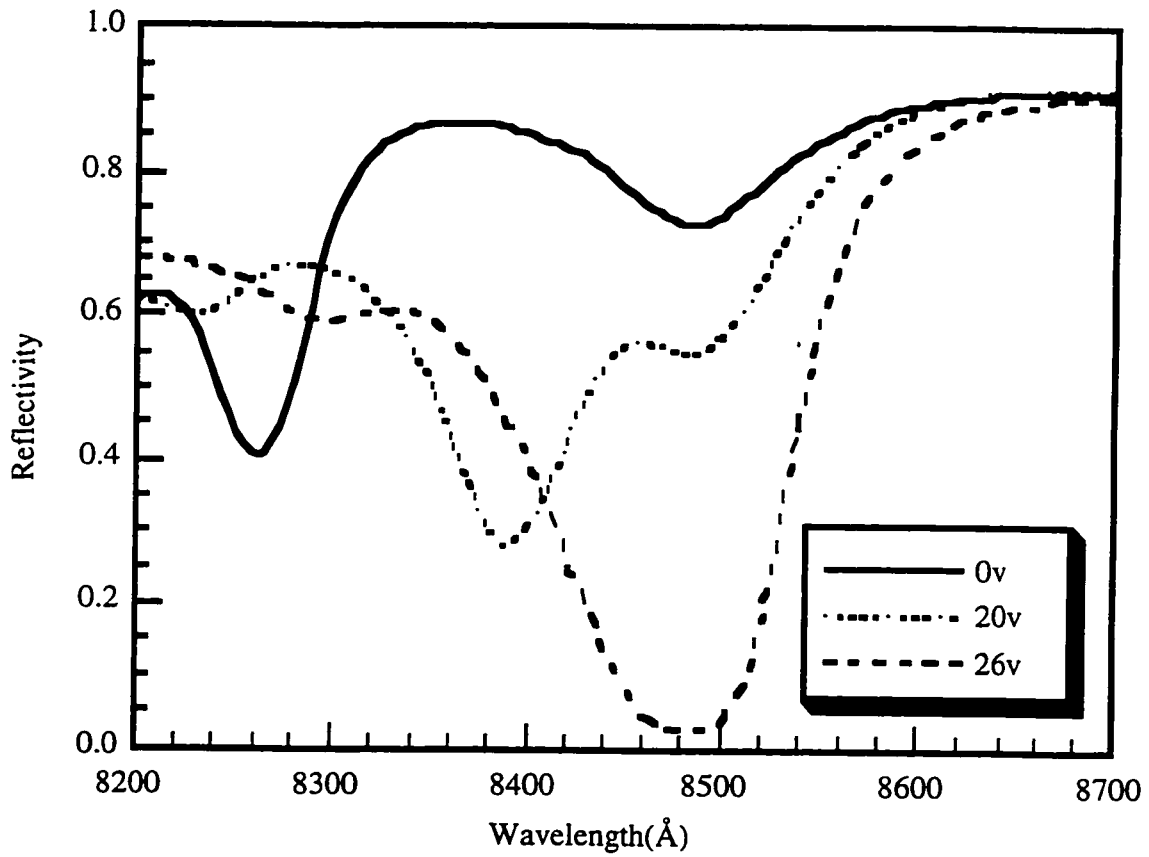

Figure 4.6 Reflectivity spectra of the anti-reflection modulator under three bias voltages.

4.5 Optical field distribution and modulation efficiency

To understand the reason for this contradiction and to find new ways to improve the optical bandwidth, the simple model has to be improved with consideration of the optical field distribution in the cavity and mirrors. Fig. 4.7 is a simulation result of the optical field distribution of the 3λ/4 anti-reflection modulator. Also shown in the same figure is the refractive index profile of this modulator as a reference, in which the region from 0μm to 2.1μm is the quarter wave stacks back mirror region, the solid black portion from 2.1μm to 2.8μm is the MQW region, and the region from 2.8μm to 3.0μm is the top 3λ/4 cavity.

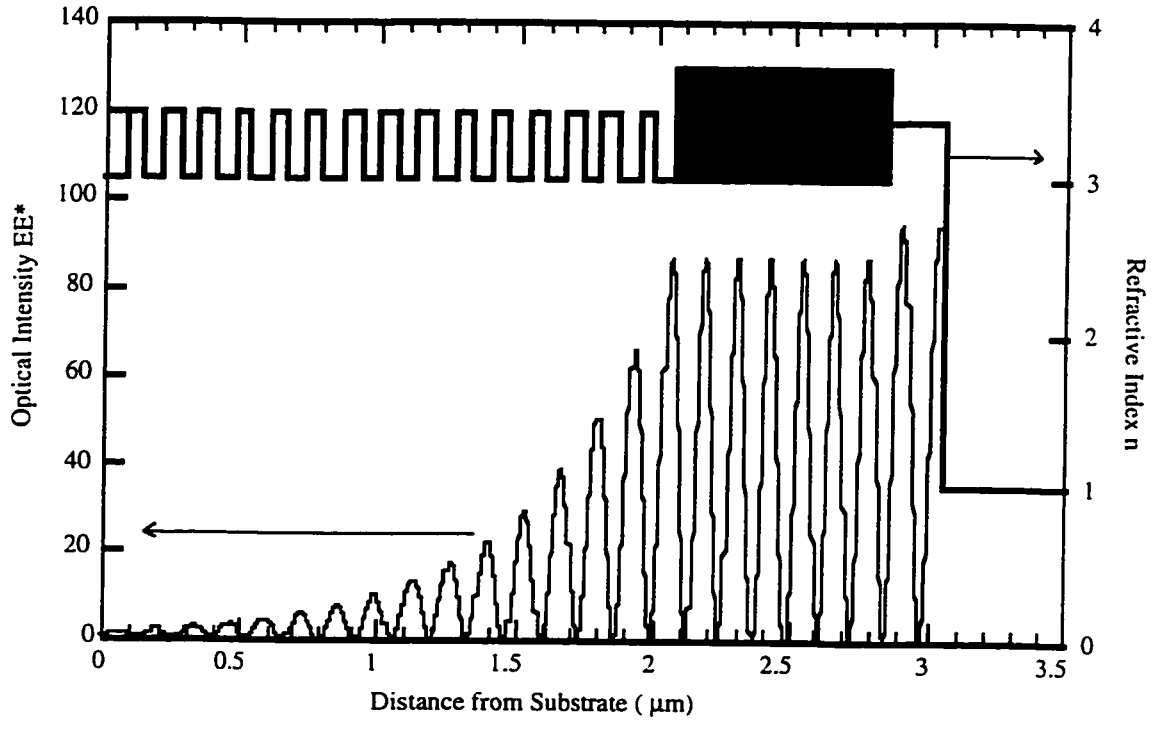

Figure 4.7 Simulation of optical field distribution in a λ/2 cavity device

As expected for a cavity, the optical field is very strong inside the 3λ/4 anti-reflection layer. However, the optical field is also very strong inside the 13λ/4 MQW layer,

and it only drops down within the $Al_xGa_{1-x}As/AlAs$ quarter wave stacks. From the optical field intensity point of view, this modulator has an effective cavity thickness, which includes the top anti-reflection layer thickness, the MQW layer thickness, and part of the quarter wave stack layers. This effective cavity thickness is much larger than the ideal cavity thickness which consists of the top layer only.

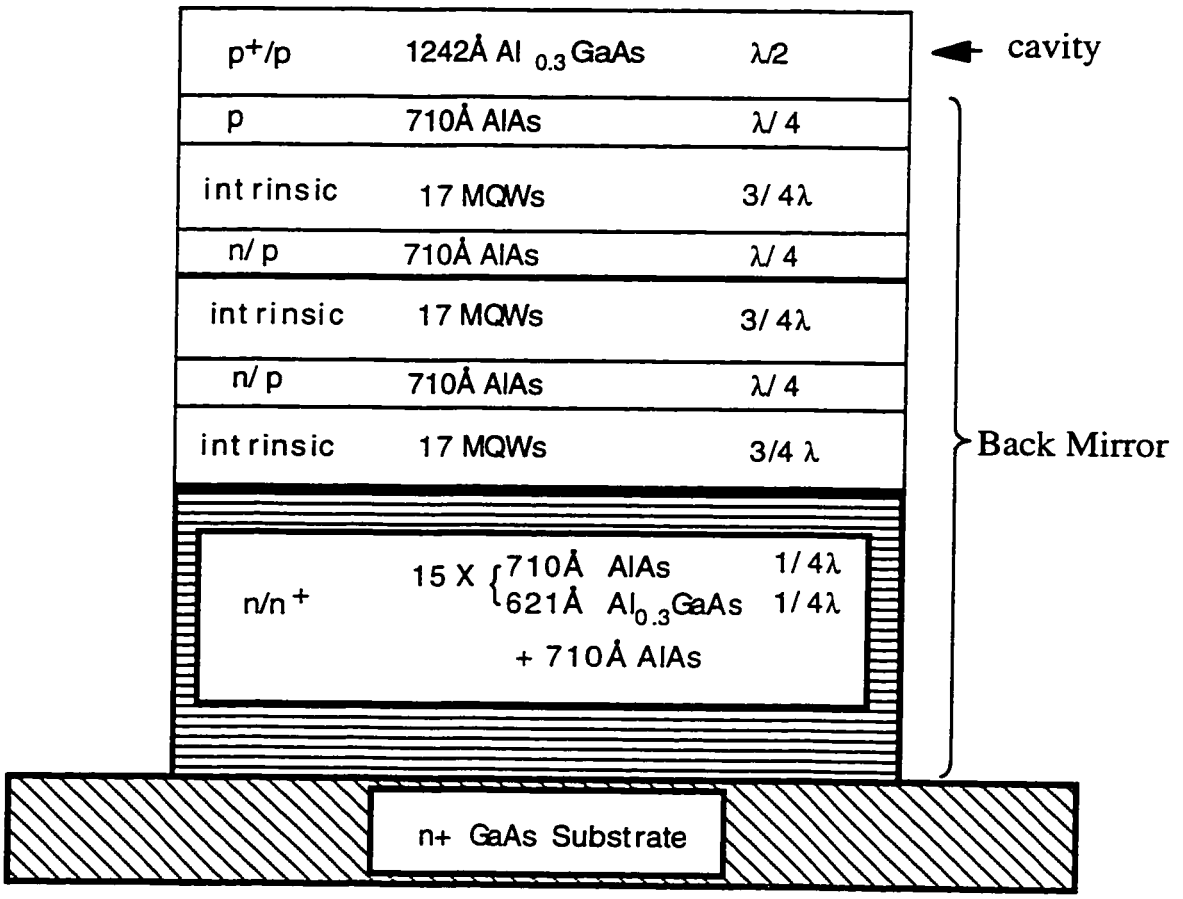

Figure 4.8 Diagram of a distributed MQW modulator structure. There are three 3λ/4 layers of MQW incorporated in the back mirror region.

The difference between this effective cavity length and the designed cavity length explains the relatively small improvements in bandwidth for both the λ/2 cavity modulator and the anti-reflection modulator over the conventional Fabry-Perot modulators. To improve the bandwidth of a short cavity modulator, the design must be improved in such a

way that the optical field is confined within the short cavity itself. This can be achieved by limiting the optical field penetration into the back mirror region. Since the MQW region has a very strong optical field, a solution is to separate this thick 13λ/4 layer into several thin quarter wave layers separated by quarter wave low index layers.

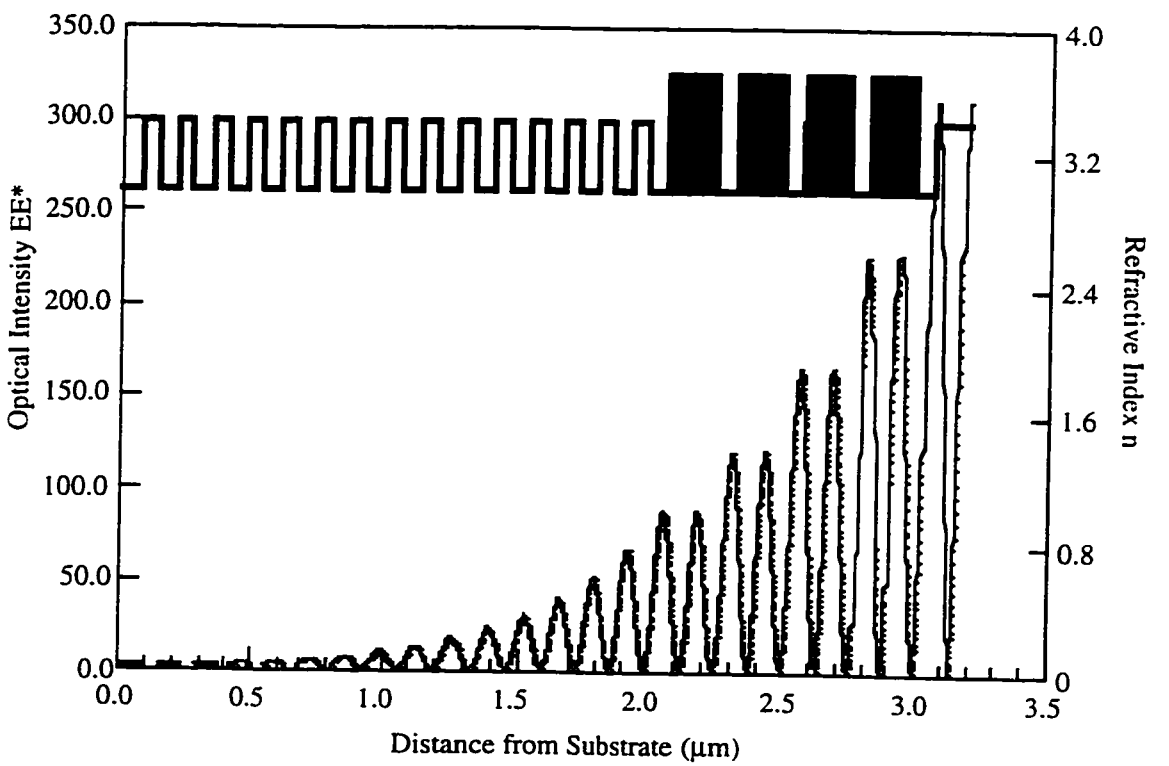

Figure 4.9 Optical field distribution in a distributed MQW modulator

4.6 Distributed MQW short cavity modulator

Figure 4.8 is a schematic diagram of a new design [60] that limits the optical field penetration into the back mirror. This modulator has a structure similar to that of the λ/2 device described earlier. The main difference, however, is that three 3λ/4 MQW layers

alternating with $\lambda/4$ low index inactive layers are used in this device in the place of a single $13\lambda/4$ MQW layer. As a side, note that each one of the two $\lambda/4$ low refractive index AlAs layers between the three $3\lambda/4$ MQW layers is doped to form a p-n junction in the middle of the layer. This doping scheme is designed to reduce voltage drops in these low index layers when a reverse bias voltage is applied on the MQW layers.

The optical field is more confined within the top $\lambda/2$ cavity since the composite back mirror now has more interfaces with different refractive indices to reflect light back to the cavity region. A simulation result of the optical field distribution in this device is plotted in Fig. 4.9. From this plot, the effective cavity thickness of this device is clearly shorter than that of the previous $3\lambda/4$ anti-reflection modulator.

Figure 4.10 is the measured modulation spectra of this device under three reverse bias conditions. The Fabry-Perot dip is very broad and shallow in the 0V reflectivity spectrum. As the voltage increases to 25V and 30V, this broad Fabry-Perot dip decreases in reflectivity with increasing exciton absorption. The modulation bandwidth of this device is 24nm, which represents a 76% increase over conventional devices with similar MQW thickness. The bandwidth is also much broader than those of the previous $\lambda/2$ cavity and anti-reflection cavity modulators.

From the spectra in Figure 4.10, it is also noted that the modulation depth of this distributed MQW device is not as good as those of the previous two short cavity devices. There are two reasons behind this degradation of modulation performance. The minor reason is the dopants in the doped low index layers between the MQW layers may diffuse partially into the intrinsic MQW layers and thus quench the QCSE effect in some of the quantum wells. This reduces the amount of absorption change and thus affects the

modulation efficiency. The main reason for the degradation of reflectivity modulation, however, is reduction of overlap between the optical field and the MQW material due to increased confinement of the optical field within the cavity. Even with the same amount of absorption change, the effective back mirror reflectivity does not change as much as in the case of a conventional Fabry-Perot modulator.

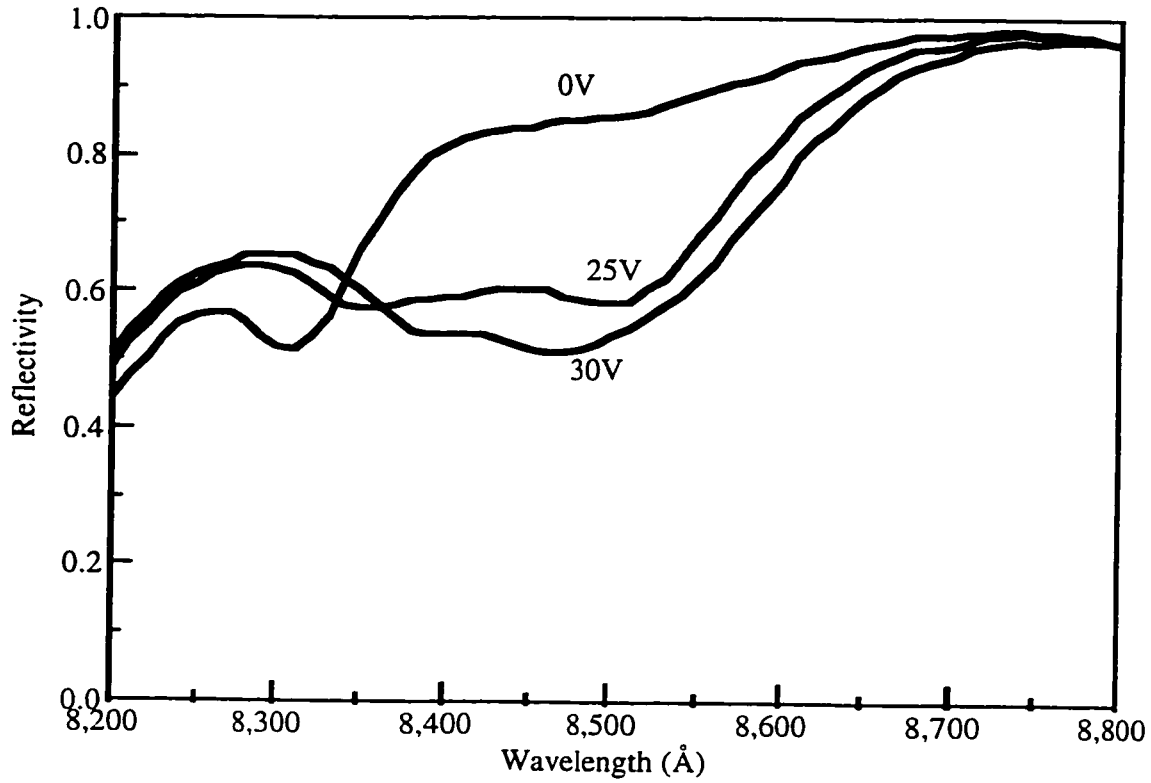

Figure 4.10 Reflectivity spectra of distributed modulator structure under three reverse bias voltages: 0V, 25V, and 30V.

This second reason reveals a fundamental compromise in this design between the modulation efficiency and the modulation bandwidth. The bandwidth is optimized when the optical field is confined within the short cavity. In the mean time, since the MQW material is placed inside the back mirror, an optical field confined inside the cavity means that there is less optical field overlapping with the MQW region. As a result, changes of absorption

due to the QCSE in the MQW layer have less effect on the total reflectivity of the modulator.

4.7 Summary

In conclusion, the optical bandwidth of a Fabry-Perot modulator depends on two factors. The first factor is the cavity length; the longer the cavity length, the narrower the bandwidth. The second factor is the mirror reflectivity; and the higher the reflectivity, the narrower the bandwidth. In traditional Fabry-Perot modulators, the cavity length is linked to the mirror reflectivity with respect to the available absorption change. Shorter cavity modulators demand mirrors with higher reflectivities. The optical bandwidth of these modulators has a maximum due to this limitation.

By moving the active MQW material into the back mirror region, the cavity can be shortened to the smallest possible length in order to enhance the modulation bandwidth. Three designs of this kind of modulators are demonstrated. There is marginal improvement over conventional devices in a $\lambda/2$ cavity modulator device. A $3\lambda/4$ anti-reflection modulator device has a slightly broader bandwidth. This work demonstrates that the effective cavity length of these devices is not just the length of the short cavity, but should also include the optical field penetration into the back mirror region. A third design with a distributed MQW back mirror improves the bandwidth at the expense of reflection modulation. We have shown that there is a compromise between modulation efficiency and modulation bandwidth in such devices due to the decrease of overlap between optical field and MQW with increasing confinement of the cavity.

5 Coupled Cavity Modulator

5.1 Motivation

In the last chapter, we discussed several ways of using short cavities to enhance the optical modulation bandwidth of Fabry-Perot modulators. As pointed out in the conclusions section of chapter 4, optical field penetration into the back mirrors of short cavity devices extends the effective cavity thickness, which then leads to narrower bandwidth. The optical bandwidth can be improved by increasing the confinement of the optical field inside the Fabry-Perot cavity, but higher confinement decreases the overlap between the optical field and the MQW material in the back mirror, and the modulation efficiency gets worse as a result. New approaches have to be investigated to improve the optical bandwidth of a Fabry-Perot modulator without sacrificing the modulation efficiency.

In this chapter, a coupled cavity structure is studied to improve the optical bandwidth of a Fabry-Perot modulator. Structurally this coupled cavity device is similar to a standard Fabry-Perot single cavity modulator. There is a top mirror and a bottom mirror.

However, instead of just one cavity in the standard modulator, this coupled cavity device has two or more cavities separated by coupling mirrors.

This configuration has been used in thin film dielectric bandpass filters [34] for three major benefits: first is to broaden the bandwidth of the high transmission band, second is to make the high transmission band more rectangular, and third is to improve the rejection outside the high transmission band. In a coupled cavity Fabry-Perot modulator [64,65,66], all these benefits are present. In addition, when compared with a single cavity device, the additional cavity provides increased flexibility in device design.

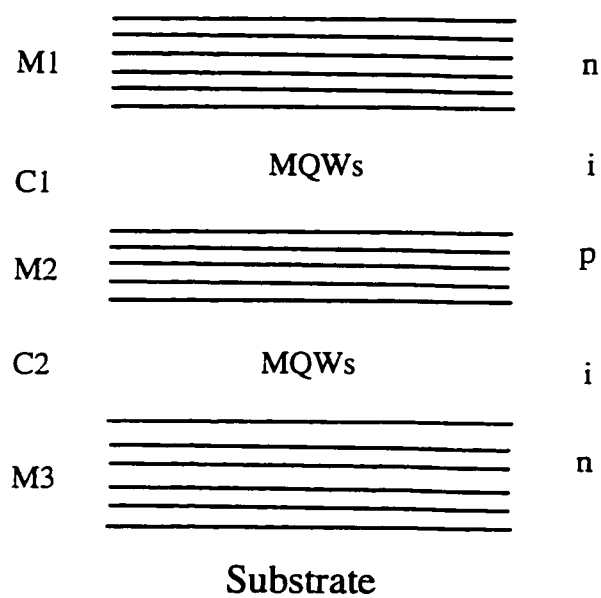

Figure 5.1 Schematic diagram of a couple double cavity device. There are three mirrors M1, M2, and M3 and two cavities C1 and C2. Each cavity has an optical thickness of an integer times $\lambda/2$.

5.2 Basic structure of a coupled cavity device

Figure 5.1 shows the schematic diagram of a coupled double cavity Fabry-Perot modulator. There are two cavities, C1 and C2, and three mirrors, M1, M2, and M3, in this device. Each of the two cavities has an optical thickness of integer multiple of $\lambda/2$. All the mirrors are doped quarter wave stacks.

Figure 5.2 illustrates the phase changes of light reflections from all three mirrors relative to the phase of incident light at the resonant wavelength. The top mirror and the bottom mirror all have π phase changes, while the middle mirror has no phase change. The balance between these three beams determines the total reflectivity of the whole device, and similar to the case of a single cavity Fabry-Perot modulator, the total reflectivity can be designed to go to zero by matching the reflectivities from these three mirrors with added absorption in either one or both of the cavities [64].

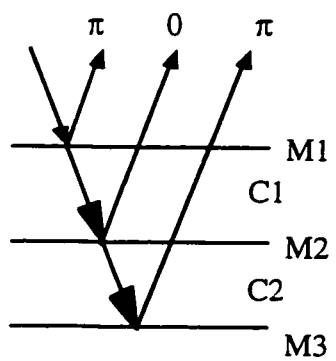

Figure 5.2 Phase relations among the reflected light beams from three mirrors in a coupled cavity structure.

Previously this coupled cavity scheme has been used in waveguide structures such as a Cleaved Coupled Cavity laser [67,68]. In that device, one semiconductor waveguide laser was cleaved into two parts, which were subsequently separated from each other by opening a small air gap. The coupling mirror in this case is the cleaved surface of the waveguides plus the air gap. Major problems with this device were that the thickness of the air gap is very difficult to be fabricated to the design specification and it was also very sensitive to environmental fluctuations.

In the vertically coupled cavity structure shown in Figure 5.1, the problems with the waveguide coupled cavity devices are avoided. The coupling mirror now is a quarter wave stack grown in one process with the rest of the structure by MBE. Because of the excellent growth rate control in MBE, the reflectivity of this coupling mirror can be accurately controlled. Since this mirror is sealed within the device, it is not sensitive to environmental changes.

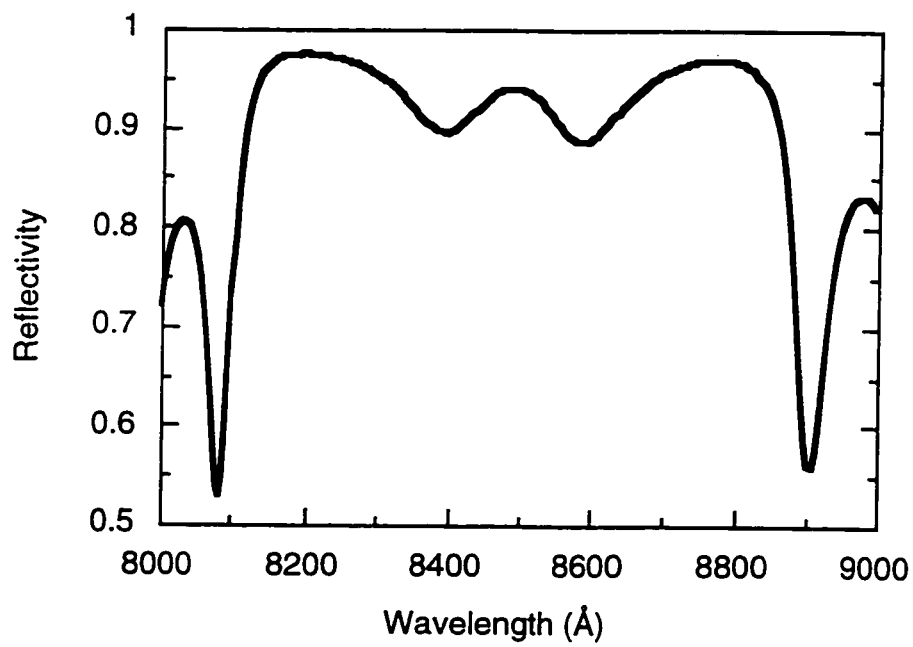

Figure 5.3 Reflectivity spectrum of a typical coupled cavity structure.

A sample reflectivity spectrum of such a vertical coupled cavity structure is shown in Figure 5.3. On top of the high reflectivity band from the quarter wave stacks, there are two Fabry-Perot dips located on both sides of the original cavity resonant wavelength at 850nm. This twin mode behavior is a direct result of the coupling between these two cavities, and the whole problem of coupled cavity modes is analogous to the coupling of electronic energy levels in a coupled quantum wells structure which is treated in basic quantum mechanics [19]. When two cavities with the same resonant wavelength are coupled together, the original degenerate single mode of each cavity couples with the other and splits into two separate modes. The spacing between these two modes depends on the coupling: the stronger the coupling, the larger the spacing.

This reflectivity spectrum is similar to the reflectivity spectrum of a traditional double cavity band pass filter, except that in the case of band pass filter, the reflectivity is close to zero near the cavity resonance wavelength, and the two Fabry-Perot dips are usually designed to be very close to form a single pass band.

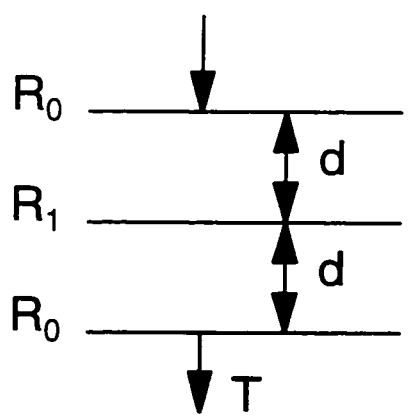

Figure 5.4 Structure of a simplified coupled cavity device.

5.3 A simple model of coupled cavity devices

A general analysis of coupled cavity structures is extremely complicated, so it is necessary to make several simplifying assumptions in order to achieve some qualitative understanding. Here we consider a simple cavity structure [69] as shown in Figure 5.4. The top and bottom mirrors are assumed to have the same reflectivity, R_0. The middle mirror has a different reflectivity, R_1. The two cavities are of equal thickness, d, and they also consist of the same material.

The mode spacing due to the coupling between these two cavities in this simple case can be derived from the general equation [69] for the total transmission through the structure:

$$T = \frac{T_0^2 T_1}{1 + R_0^2 + 4R_1R_0 - 4\sqrt{R_1R_0}(1 + R_0)\cos 2\phi_0 + 2R_0 \cos 4\phi_0} \tag{5.1}$$

in which $T_0 = 1 - R_0$, $T_1 = 1 - R_1$, $\phi_0 = \frac{4\pi nd \cos\theta}{\lambda}$, and θ is the incident angle of light.

The wavelength range between the two maxima of transmission is the modal splitting spacing, and it is given by:

$$\Delta\phi = \sqrt{2}\left(1 - \frac{\sqrt{R_1R_0}(1 + R_0)}{2R_0}\right)^{\frac{1}{2}} \approx \sqrt{T_1} \tag{5.2}$$

and the last part of this equation is true under the condition of $R_0 = 1$ and $R_1 \approx 1$. So the modal splitting increases with increasing coupling, i.e., the stronger the coupling, the wider the splitting.

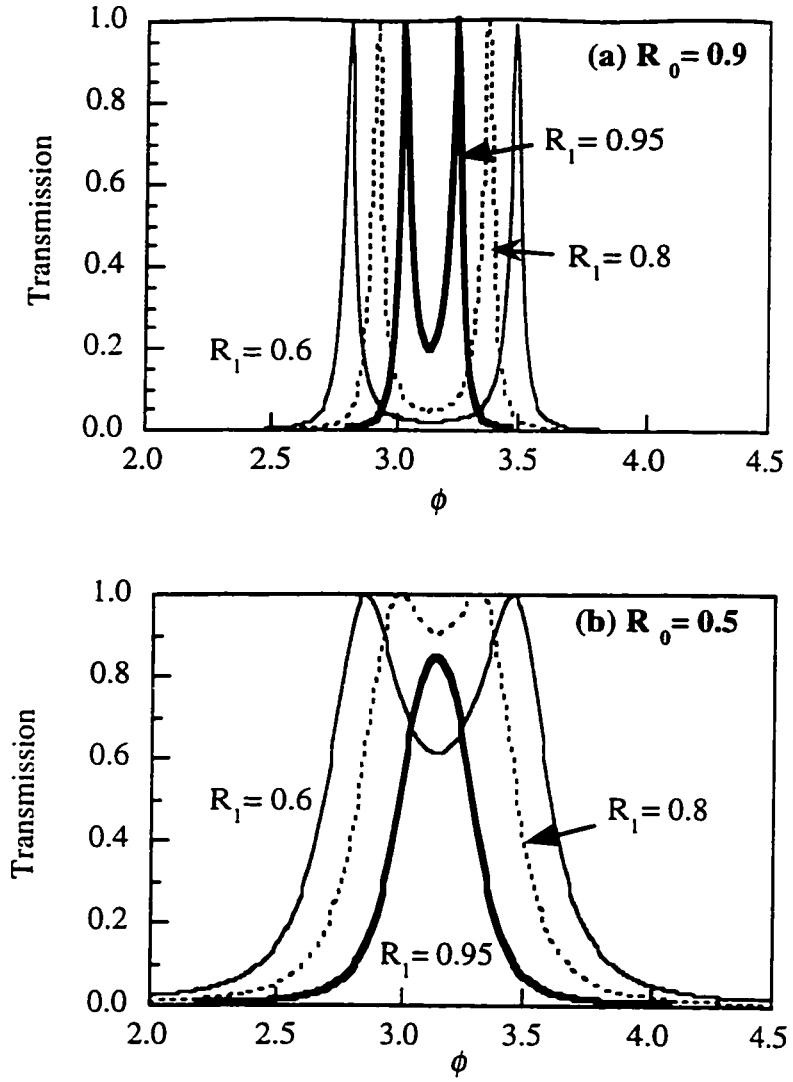

Figure 5.5 Reflectivity spectra of two sets of simple coupled cavity structures. The three curves in each graph correspond to center mirror reflectivities of 60%, 80% and 95% respectively. All three devices in (a) have 90% reflective front and back mirrors. All three devices in (b) have 50% front and back mirrors.

Figure 5.5 further illustrates the relation between mode splitting and the middle mirror reflectivity. In Figure 5.5 (a), all three structures have 90% reflective front mirrors and back mirrors, but the middle mirrors have reflectivities of 60%, 80%, and 95%. When we compare the mode splitting, it is clear that the splitting decreases as the middle mirror reflectivity increases. The structures shown in Figure 5.5 (b) are different from those in

Figure 5.5 (a) only by the front and back mirror reflectivities, which are now 50%. The mode splitting also shrinks with increasing middle mirror reflectivity, which is similar to Figure 5.5 (a).

One additional detail, however, is that when the middle mirror is 95% reflective, the mode splitting becomes zero, i.e., there is now only a single Fabry-Perot mode in the reflectivity spectrum. This single mode behavior is caused by the high reflectivity of the middle mirror, which decouples these two cavities into two individual cavities acting independently and in optical series.

In this simple coupled cavity model, the single Fabry-Perot mode condition [66] can be derived from equation (5.2) as when $\Delta\phi = 0$:

$$R_1 \geq \frac{4R_0}{(1+R_0)^2} \geq R_0 \tag{5.3}$$

In other words, if the middle mirror is less reflective than the front and back mirrors in a coupled cavity structure, there is always a splitting of Fabry-Perot modes. If the back mirror has a high value, it may be practically impossible to achieve the single mode condition because of the even higher middle mirror reflectivity required.

5.4 Coupled cavity modulator

There are two possible designs of coupled cavity modulators. One is a single mode modulator with mirror reflectivities satisfying equation (5.3), the other is a split mode modulator. The first design has a single broad Fabry-Perot dip, while the second design has two separate Fabry-Perot dips. Due to the high reflectivity required for the middle mirror in the first design, it is difficult to achieve broad bandwidth. For this reason we have concentrated on the second design.

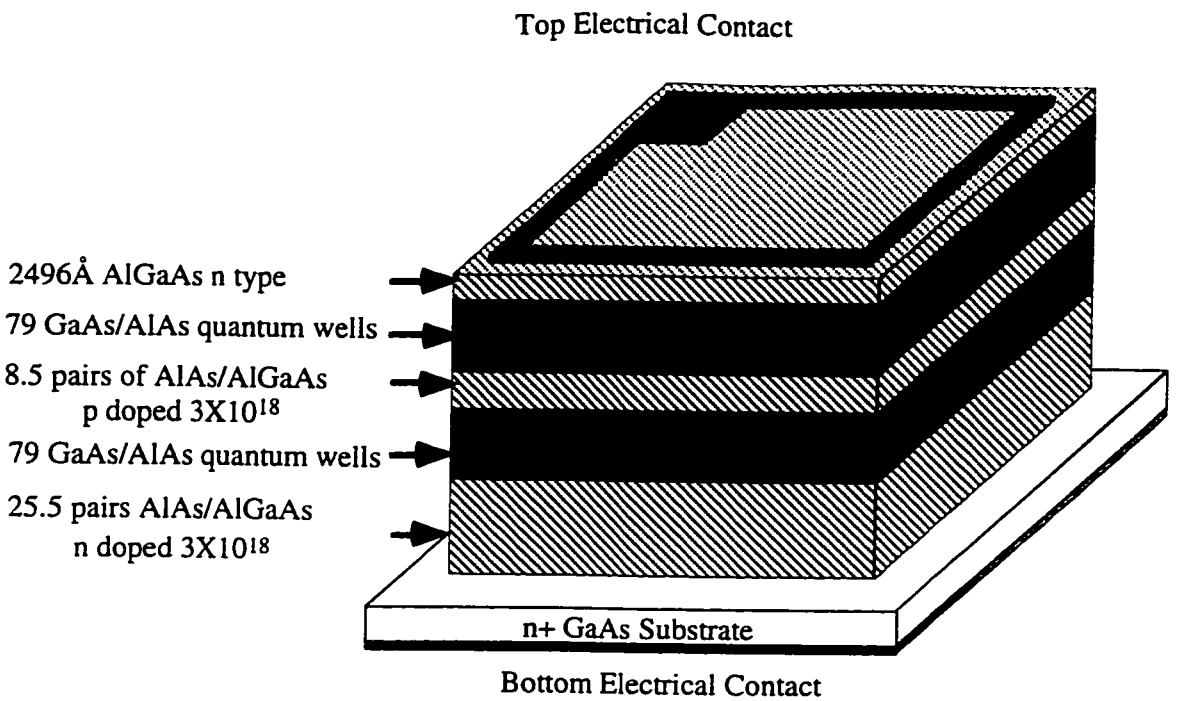

Figure 5.6 Structural diagram of a coupled cavity modulator.

Fig. 5.6 is a schematic diagram of the device structure of such a strongly coupled double cavity modulator, in which there are two identical GaAs/AlAs MQW cavities of $8\lambda/2$ optical thickness. The back mirror and the middle mirror consist of quarter wave stacks of 25.5 pairs and 8.5 pairs, respectively. A contact and protection $Al_xGa_{1-x}As$ layer is grown at the top of the top cavity. The front mirror is just the interface between this layer and air, which has a reflectivity of about 30%. The only two electrical contacts on this device are to the bottom substrate and the top layer. Due to the doping scheme, only one of the cavities is under reverse bias depending upon how the whole device is electrically biased. The other cavity is forward biased, so there is little voltage drop across it. The absorption inside that cavity does not change very much during the modulation process.

Fig. 5.7 shows the modulation spectra of this modulator under different reverse bias voltages on the top cavity. There are two Fabry-Perot dips on the high reflectivity

band in the 0V spectrum. The exciton absorption peak is originally at around 825nm and overlaps with the edge of the high reflectivity band. At 35V, the exciton peak shifts to the wavelength of the first Fabry-Perot dip, 835nm, and the increase of absorption at this wavelength decreases the total reflectivity to almost zero. When the voltage increases to 42V, the exciton peak is now shifted further to the second Fabry-Perot dip wavelength of 849nm. The total reflectivity at this wavelength is now at a minimum of 10%. Since the absorption peak has passed the first Fabry-Perot dip wavelength, the reflectivity there rebounds a little bit, but the overall reflectivity change and contrast ratio is still very good. So in this modulator, we have achieved good modulation at two bands of wavelengths centered around 835nm and 849nm. The total usable bandwidth is effectively twice the amount of a conventional modulator with a comparable cavity thickness.

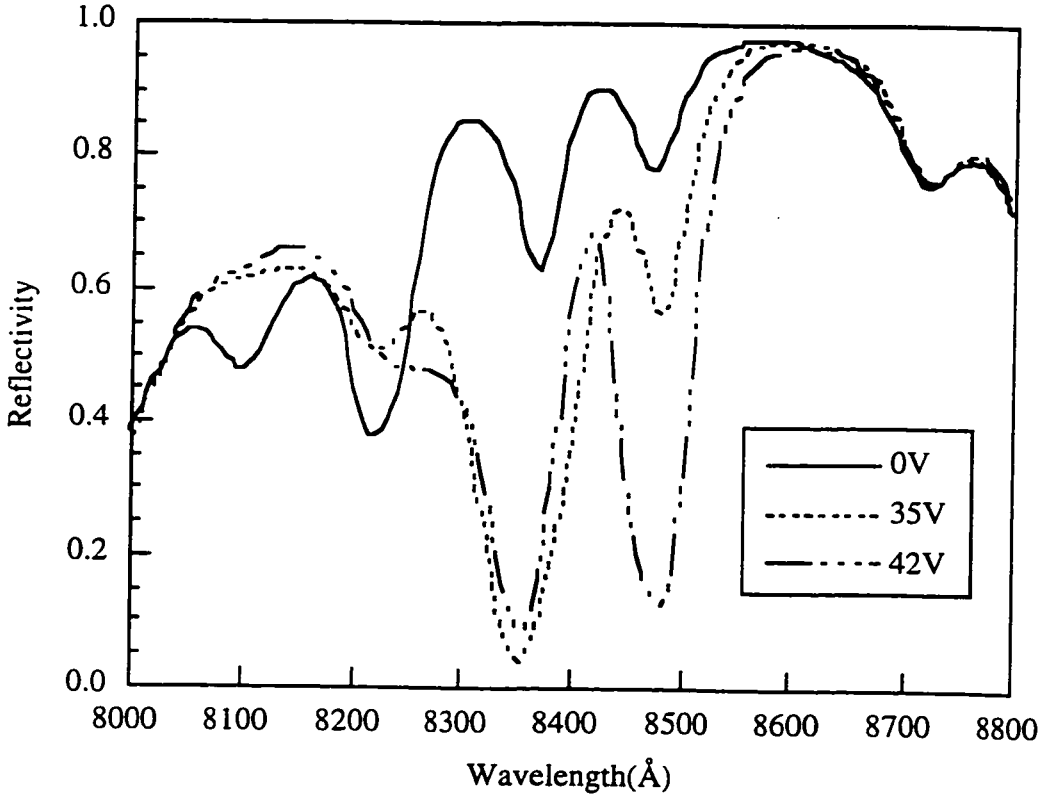

Figure 5.7 Reflectivity spectra of the coupled double cavity modulator

5.5 Summary

In summary, coupled cavity modulators are used to expand the optical modulation bandwidth of conventional Fabry-Perot modulators. These coupled cavity modulators have two or more cavities coupled via mirrors between them. The original degenerate single cavity mode splits into many modes whose exact number equals to the number of cavities. The amount of splitting depends on the coupling between these cavities. Stronger coupling results in larger splitting. When the coupling mirror is sufficiently strong, there can be only one mode present in the reflectivity spectrum. For broad bandwidth Fabry-Perot modulators, however, the double dip design is better than the single design since it does not require a strong middle mirror. We have demonstrated a coupled cavity modulator with good optical bandwidth around 835nm and 848nm under 42V bias voltage. The modulation depth of this kind of double cavity modulators is similar to that of the single cavity Fabry-Perot modulators. The phase property of these modulators is also similar to that of the single cavity device in the case of all cavities have identical MQW material. It is possible to improve the phase performance of the double cavity modulators by carefully designing different MQW for different cavities.

6 Coupled Cavity Modulator and Light Emitting Diode

6.1 Introduction

In chapter 5, coupled cavity structures are shown to be capable of enhancing the bandwidth of modulators. This approach is based upon the understanding that a separate light source will be used together with the modulator. Aligning the wavelength of this light source to within the bandwidth of the modulator is critical for the application. However, if we can integrate a light source and a modulator into one device, and manage the wavelength alignment between the modulator and the light source device during the design process of this integrated device, we can circumvent this wavelength alignment problem completely. This is the motivation behind the design discussed in this chapter, which integrates a light emitting diode and a transmission Fabry-Perot modulator in a coupled cavity configuration.

Traditionally, all optical communication systems have used one of three kinds of devices as their signal sources [40 70]: directly modulated lasers, directly modulated light emitting diodes, or modulators working together with lasers/light emitting diodes running

at constant output power. Each of these three sources has its advantages and disadvantages. Table 6.1 lists the major advantages and disadvantages associated with them.

	Advantages	**Disadvantages**
Directly modulated laser	High speed ~10 GHz High optical power ~100 mW Narrow linewidth ~0.1nm One device	High cost High chirp Relatively short lifetime Sensitive to environment change
Directly modulated LED	Low cost Long lifetime One device	Low speed ~200 MHz Low optical power ~100 μ W Broad linewidth ~ 40nm
Modulator + laser/LED	High speed ~30 GHz Long lifetime (Modulator)	Two devices (require spatial alignment and wavelength alignment) Bandwidth is broad for LED

Table 6.1 Advantages and disadvantages of three optical communication signal sources.

An integrated light emitting diode and modulator device has all of the benefits of the modulator + LED system, but solves both the spatial and wavelength alignment problems in the integrated design. The spatial alignment is trivial in an integrated vertical device since one device is grown right on top of the other in one step during the material growth. Since only the non-critical lateral dimensions of these devices need to be defined by the optically rough lithographic and etching process which can degrade optical performance. The built-in alignment of wavelength in an integrated device is only limited by the design since the growth accuracy is very high in terms of thickness and composition control in modern

growth techniques such as MBE. Therefore, combining the modulator and the light source in one device is a promising solution to the alignment problems. Such a device has the potential to reach electrical modulation speeds much higher than a directly modulated LED system. The lifetime of this integrated device should be comparable to a directly modulated LED, which is quite long. In addition, this device is cost-effective compared to the conventional two device scheme, since no alignment is needed.

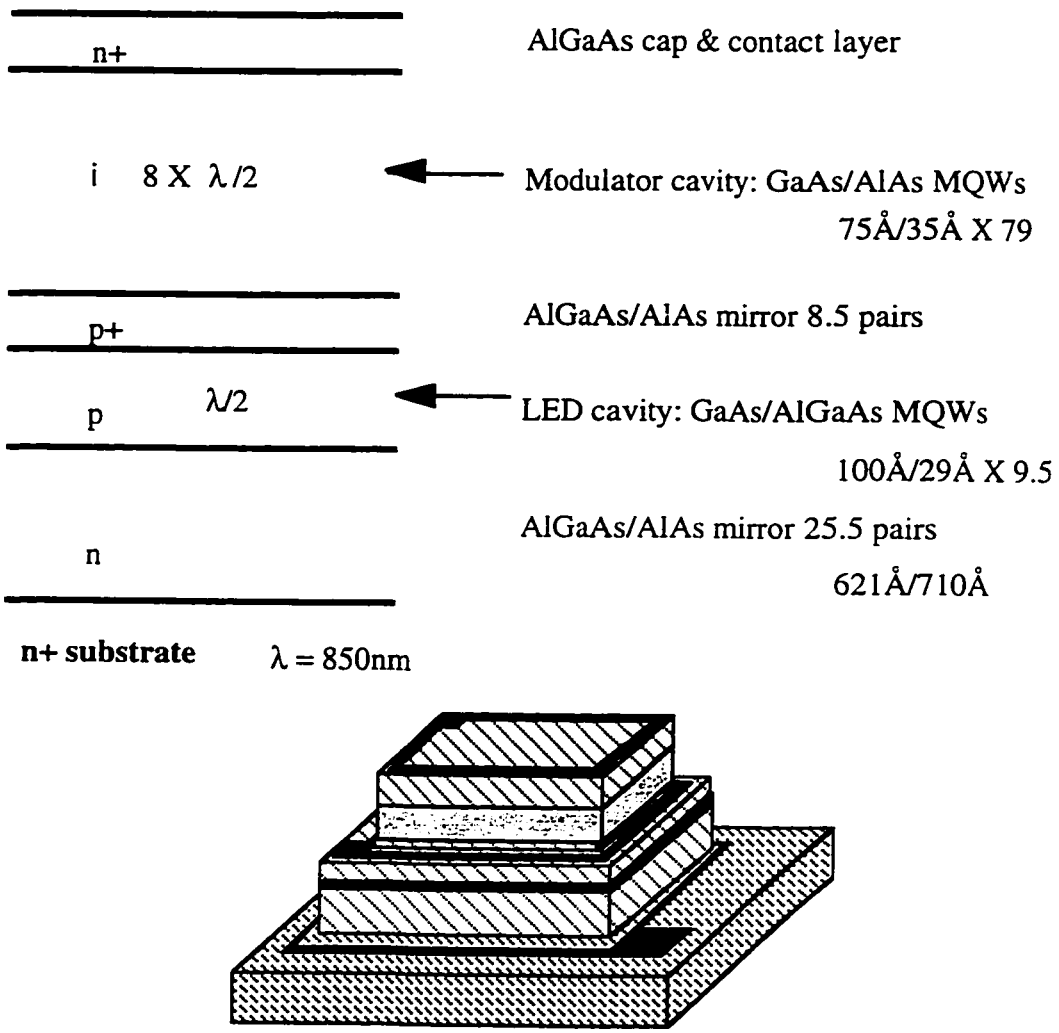

Figure 6.1 Structure of an integrated LED and Modulator.

6.2 Device structure

We have grown and tested an integrated modulator and LED device. The device structure is illustrated in Fig. 6.1. This integrated device was grown by MBE on an n doped GaAs substrate. It starts with a 25.5 pair n doped AlAs/$Al_{0.3}Ga_{0.7}As$ quarter-wave stack back mirror, followed by 9 periods of lightly p doped GaAs/$Al_{0.3}Ga_{0.7}As$ multi-quantum wells (MQW) acting as the active region of an LED. The optical thickness of this LED layer is 425nm, one half of the operating wavelength. We used another 8.5 pairs of p doped AlAs/$Al_{0.3}Ga_{0.7}As$ quarter wave stacks between the LED active region and the modulator MQW region. The function of this layer is two-fold: First, its reflectivity determines the coupling between the two cavities it separates; Second, it provides an electrical contact layer so that each of the two cavities can be electrically biased independently.

On top of the middle mirror is the second cavity, which is the modulator. It has 79 periods of undoped GaAs/AlAs MQW with an optical thickness of 8 times $\lambda/2$. A final n doped $Al_xGa_{1-x}As$ layer for contact finishes the device. We processed this device into a double mesa structure, as shown on the bottom of Figure 6.1, then deposited metal contacts onto the top contact layer, the middle mirror layer, and the backside of the wafer, in order to control both the modulator and the light emitting diode independently.

6.3 Results

We tested this device in three different operating modes. First, we measured its reflectivity spectra under different bias conditions on the top modulator cavity, as plotted in Figure 6.2. The LED is idle for this measurement.

In the zero-bias spectrum, there are two distinctive Fabry-Perot dips at 845nm and 855nm on top of the high reflectivity band, which extends from 830nm to 870nm. These

dips come from the resonant coupling between the two cavities of the LED and the modulator. The spacing between the two dips is mainly determined by the reflectivity of the middle mirror. As discussed in Chapter 5, when the reflectivity of the middle mirror is high, these two cavities are weakly coupled and their optical modes degenerate, which leads to one single Fabry-Perot dip on the reflectivity curve. When the reflectivity of the middle mirror is low, the coupling between cavities is strong and thus the cavity modes push each other apart. In this device, we chose to use a relatively strong coupling mirror since this configuration is less stringent on growth accuracy. A weakly coupled middle mirror is useful when integrating a Vertical Cavity Surface Emitting Laser (VCSEL) with a modulator in a coupled cavity structure, because the two cavities should definitely be de-coupled so as to eliminate any feedback into the VCSEL due to any change of either absorption or refractive index in the modulator cavity. This feedback coupling is not an issue for the coupled LED/modulator device.

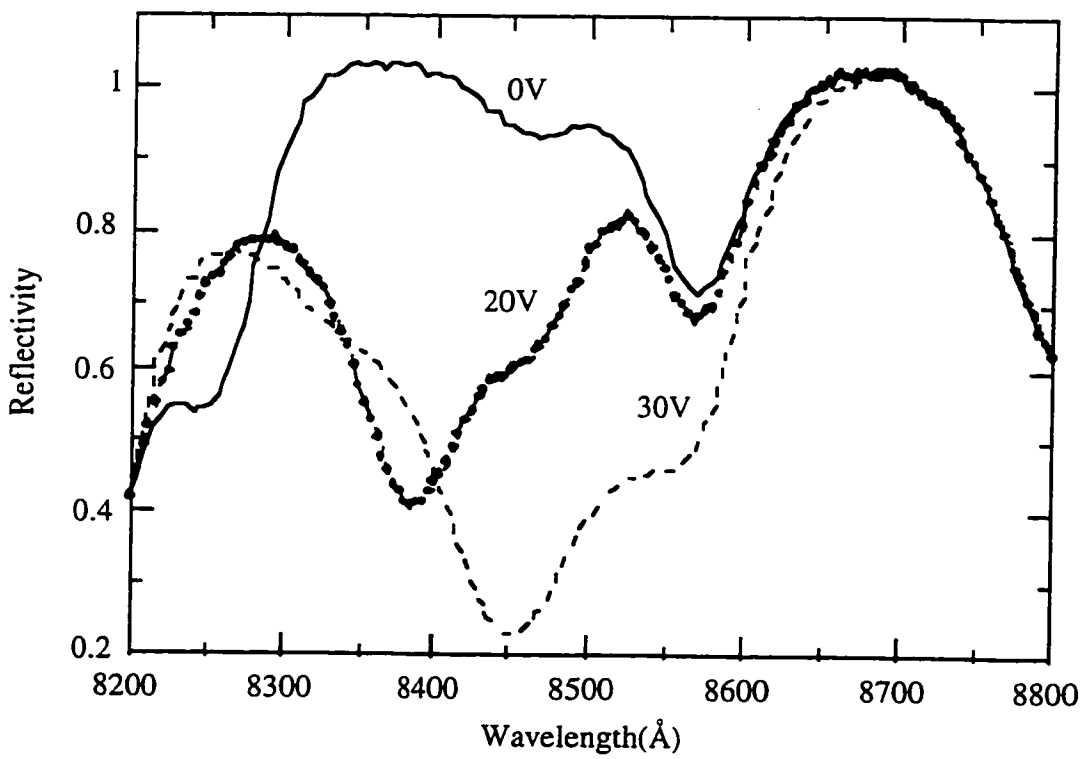

Figure 6.2 Reflectivity spectra of the integrated device.

When the bias is increased to 20V, the exciton absorption peak shifts to 838nm. The reflectivity at the first Fabry-Perot dip at 845nm drops down to 70% due to the increased absorption. There is minimal change of reflectivity for the other Fabry-Perot dip at 855nm.

At 30V bias voltage level, the exciton peak overlaps with the first Fabry-Perot dip at 845nm. Reflectivity at this wavelength is at a minimum of 22%. The reflectivity at the second Fabry-Perot dip at 855nm is 46%. All these indicate that this device is a good reflection modulator with a broad optical modulation bandwidth.

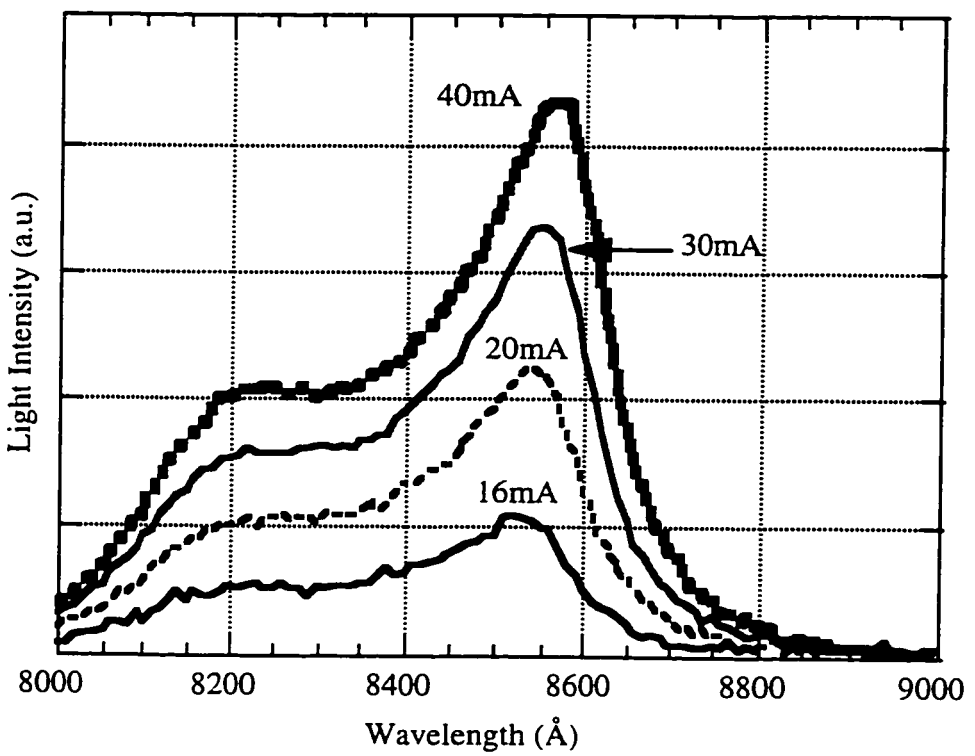

Figure 6.3 Light emitting diode output light intensity spectra under different current injection levels.

We next tested the performance of the light emitting diode in a test LED device, which has the same structure as the LED in the integrated device, but without all the mirrors. Fig. 6.3 shows the output light intensity of this test LED versus wavelength under

different current injection levels. No voltage was applied on the Fabry-Perot modulator cavity. When the current injection level increases, the light output intensity increases. The small red shift of the emission peak wavelength at 40mA from the one at 16mA indicates good thermal contact between the integrated device and the substrate even without any special treatment.

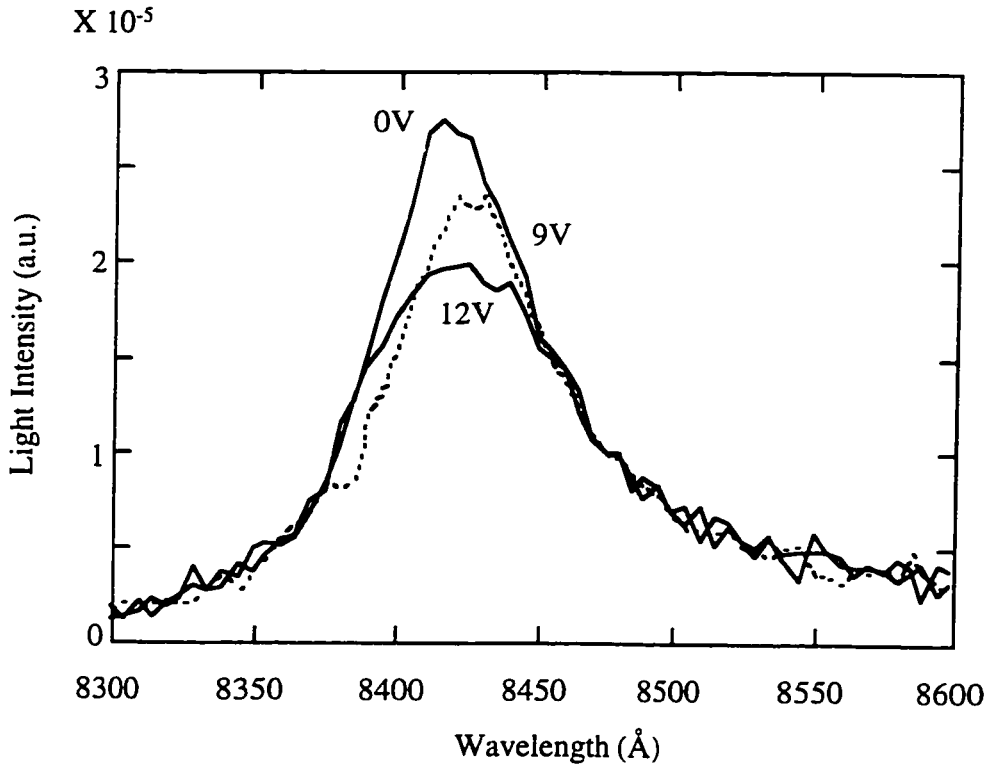

Figure 6.4 Output light intensity spectra under different bias voltages of the modulator in the integrated device. The current of the LED is fixed.

To demonstrate the modulation characteristics of the integrated LED and modulator device, we injected the LED with a constant current source and measured the output light spectra under different bias voltages on the modulator. The measurement results of total output light intensity spectra is shown in Fig. 6.4. The injection current of the LED is fixed at a constant level while the modulator voltage changes from 0V to 9V. With this 9V

voltage swing, the total light output decreases by about 30%. The result demonstrates that this integrated coupled-cavity device can be used as a signal source as designed.

The linewidth of emission in this integrated device is about 7.5nm, which is much narrower than the linewidth of the test device shown in Figure 6.3, which is 43nm. This narrow down of linewidth is caused by the Fabry-Perot cavity, and has been used to make resonant cavity light emitting diodes [71,72,73] which has very narrow linewidth than conventional LEDs. This narrow linewidth helps to increase the communication distance at high transmission speed which is limited by the chromatic dispersion of optical fiber.

The modulation depth of 30% for this device, however, is not optimal. There are two possible reasons for this relatively low performance. First, the bias voltage applied to the modulator with the LED turned on was not as high as when the LED was off. This is because the MQW material we used has a low saturation intensity [74,75] as a result of the high potential barrier of the AlAs layers. A possible solution to this problem is to use a lower barrier $Al_xGa_{1-x}As$ material to replace the AlAs in the MQW material to achieve higher saturation intensity.

A second possibility for the low modulation depth of this device is a mismatch between absorption and transmission. For the modulator, the sum of transmissivity, absorptivity, and reflectivity equals unity due to the law of energy conservation:

$$R + T + A = 1 \tag{6.1}$$

in which R is the reflectivity, T is the transmissivity, and A is the absorptivity. Absorptivity A is determined by the QCSE of the MQW material. It changes from 0 to A_{max} as the electric field on the MQW increases. In an integrated device of LED and modulator, the change in transmissivity T is the parameter that needs to be optimized with respect to the available absorptivity change.

In the design of our tested device, the maximum Fabry-Perot transmission state correspond to the maximum absorption state inside the modulator cavity. The reflectivity of this device is at minimum. When the absorption is low, the reflectivity was designed to be at a high value, and in this condition the transmission is relatively low also. So the change of reflectivity in this design was maximized, but the transmission change was not. Even with this design characteristics, we were still able to observe enough transmission modulation to demonstrate the basic operating principle of the integrated device.

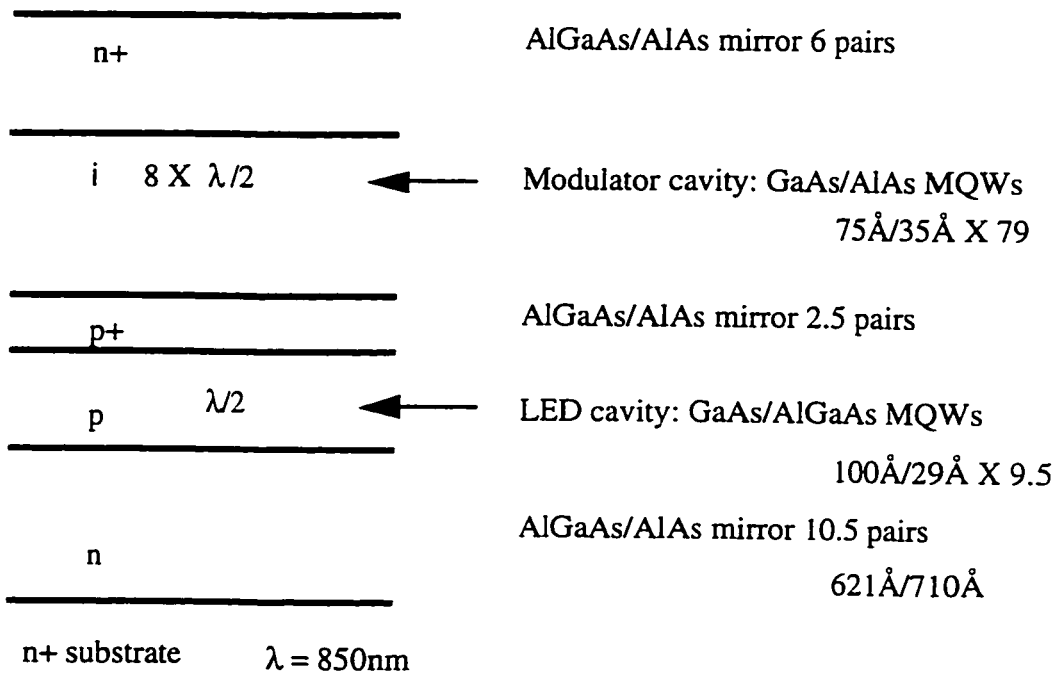

Figure 6.5 Structure of an improved coupled cavity LED/Modulator device with optimized transmission change.

6.4 Improvements in transmission change of a modulator

From theoretical simulations, we expect to improve the modulation ratio to 20:1 after adjusting the maximum transmission state to correspond to the minimum absorption state. The optimized device is another coupled cavity structure as illustrated in Figure 6.5.

Compared with the original design, this device has a stronger front mirror, a weaker back mirror, and a weaker middle mirror to increase coupling. In this device, when the absorption is low, the reflectivity is also designed to be low, and the transmission is high according to equation (6.1). When the absorption is high, the reflectivity increases simultaneously, and the transmission is very low, also according to equation (6.1). The simulated results of the transmission spectra under both the lowest and the highest absorption levels are plotted in Figure 6.6.

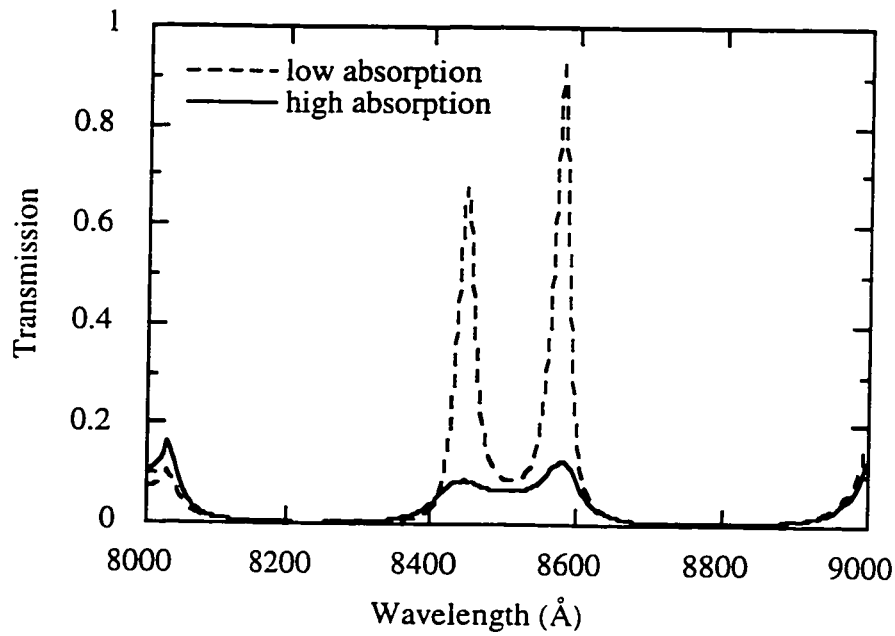

Figure 6.6 Transmission spectra of an improved coupled cavity design under the lowest and the highest absorption levels inside the modulator cavity.

The transmission is peaked at 845nm and 858nm under the low absorption condition. When the absorption level is high, the transmission at both wavelengths drops down to about 10%. Because the structure of this improved device is essentially the same as the original, and the changes are only made in the number of mirror stacks, it is expected that the simulation result of this device is a good indication of the potential performance of a real device, which should be much better than the original device.

6.5. Summary

We have demonstrated a vertically integrated coupled cavity device consisting of a LED and a transmission Fabry-Perot modulator. As a signal source in optical communication systems, this device combines the advantages of a directly modulated LED source and a signal source consisting of a discrete modulator working together with a LED driven at a constant power level. It has the speed advantage of a discrete modulator (tens of GHz) over the directly modulated LED (hundreds of MHz) and the long life time of a LED device when compared to the directly modulated laser source. In addition, as an integrated device, it eliminates the alignment problems associated with the discrete modulator plus LED source. Both the simulation and the experimental data indicate that this device is promising for high speed, low cost , long lifetime, short distance optical communication applications.

7 Conclusion

7.1 Summary

Two important performance characteristics of asymmetric vertical cavity Fabry-Perot MQW reflection modulators were studied in this thesis. The first one is the phase characteristics of these modulators, which is a limiting factor in the high speed performance of these Fabry-Perot modulators. Similar to a Fabry-Perot filter, any change of the refractive index inside the Fabry-Perot cavity shifts the cavity resonant wavelength, and leads to gradual phase change at the original cavity resonance wavelength. However, due to the absorption within the cavity in a Fabry-Perot modulator, its phase property is more complicated than that of a Fabry-Perot filter. Whenever the absorption inside the cavity changes from one side of the impedance matching condition level to the other side, the phase of reflected light at the cavity resonance wavelength shifts 180°. In chapter 3, we demonstrated a modified Michelson interferometer set-up to accurately characterize the phase properties of a Fabry-Perot modulator. The results show that away from the cavity resonant wavelength, the phase of reflected light has only a slight change as the absorption changes inside the cavity. However, near the cavity resonance, the phase changes

drastically due to the influences of both refractive index change and absorption change inside the cavity.

The second important Fabry-Perot modulator performance factor is the optical modulation bandwidth. Broad bandwidth modulators are desirable not only in improving both the design and manufacturing tolerance of Fabry-Perot modulators, but also in improving the reliability of a communication system that includes a narrow linewidth laser source and a Fabry-Perot modulator.

The optical bandwidth of a Fabry-Perot cavity depends on two factors. The first is the cavity length and the second is the cavity loss, which is the combination of the absorption inside the cavity and the mirror reflectivity. In general, short cavity length and low mirror reflectivity lead to broad bandwidth. However, in traditional Fabry-Perot modulators, short cavity length requires high mirror reflectivity due to the limited absorption change available from the QCSE. In chapter 4, we demonstrated three designs of short cavity modulators in which the MQW material is moved to the back mirror region and the cavity consists only of inactive $Al_xGa_{1-x}As$ material. The first two designs used $13\lambda/4$ MQW layers embedded in the back mirror and $\lambda/2$ high refractive index cavity and $3\lambda/4$ medium index cavity structure. The modulation bandwidth of these modulators does not improve significantly over the conventional modulator due to the elongated effective cavity length caused by the optical field penetration into the back mirror region. In the third design, a distributed structure of three $3\lambda/4$ MQW layers separated by low index $\lambda/4$ layers is used as the back mirror under a $\lambda/2$ cavity. The bandwidth of this device shows marked improvement with some degradation of modulation depth. This degradation indicates a design compromise between the optical bandwidth and modulation depth that is inherent to these types of devices.

In chapter 5, we investigated another approach to increase the optical bandwidth of a Fabry-Perot modulator by adding another cavity to the structure. Due to the coupling between the two cavities, the original Fabry-Perot mode separates into two modes, and the optical bandwidth can be doubled by modulating both modes. The coupling is controlled by the middle mirror reflectivity with stronger reflectivity giving weaker coupling and vice versa.

We demonstrated an integrated light emitting diode and Fabry-Perot modulator device in chapter 6. This device avoids the optical bandwidth problem of Fabry-Perot modulators by pre-aligning its operating wavelength with the wavelength of a light emitting diode in the design. This kind of device also has the potential of high speed operation of over 10 GHz and long operational lifetime. We achieved 30% modulation of the output light from LED at 841nm in a test device. With improved matching of absorption and transmission in the modulator, we believe the modulation ratio could be improved to 90%.

7.2 Future work

Optical modulators, especially those that can be integrated with silicon ICs, are promising in improving the data communication speed among different computer boards or even different computer chips on the same board. The integrated coupled cavity device is a suitable candidate for this application for two reasons. First, it is a complete signal source that can be easily driven by standard CMOS circuits. Second, it is a vertical device, which means that dense two dimensional arrays can be fabricated and their output light can be easily coupled into optical fibers which then connect to other devices. A few of the important directions for the future are outlined in the following paragraphs.

Absorption and transmission matching in an integrated modulator and LED . As shown in chapter 6, the absorption inside the modulator needs to be matched to the

transmission to maximize modulator performance. Specifically, the absorption maximum should overlap with the minimum in transmission and the absorption minimum should overlap with the maximum in transmission. This can be achieved by both increasing the reflectivity of the front mirror and adjusting the middle mirror reflectivity accordingly in a coupled cavity structure to enhance the resonance within the top modulator cavity. Another possibility is a bottom emitting configuration, in which the top cavity is the light emitting diode cavity and the bottom cavity is the modulator cavity. Wafer bonding techniques may be used to bond a LED device on top of a modulator device, and in this case highly reflective dielectric optical coating can be used as the middle mirror and the back mirror of the LED to enhance both the output efficiency of the LED and the resonance of the modulator.

Integrated VCSEL and modulator . A VCSEL has several advantages over a LED, which makes them more desirable in communication systems. These advantages include: higher power output, better efficiency, and narrower linewidth. When a VCSEL is integrated with a Fabry-Perot modulator, the modulation speed of this integrated device is determined by the speed of the modulator, which can be much faster than the speed of a directly modulated VCSEL. Potential problems in such an integrated device are complex optical design and precise material growth. The optical field inside a laser diode is sensitive to external feedback, which will certainly be present in this integrated configuration during the modulating process. However, using a highly reflective middle mirror may isolate the laser cavity from the modulator cavity. Another potentially useful configuration is to utilize this external feedback to achieve mode locking of the VCSEL and to produce extremely short pulses. One potential problem for this integrated structure is that the thickness of a VCSEL is typically around 4μm and the thickness of a Fabry-Perot modulator is around 2μm. The total thickness of the integrated device is approaching the limitations for the commonly used growth techniques, MBE or MOCVD, due to the growth rate

fluctuations which can occur during the very long growth time. This problem may be solved by in-situ growth rate monitoring and adjustments.

References

1. S.M. Sze, *Physics of Semiconductor Devices* , (John Wiley & Sons, New York, 1981).

2. U. Efron, *Spatial Light Modulator Technology: materials, devices, and applications,* 665 (Marcel Dekker, New York, 1995).

3. Y. Yamamoto & T. Kimura, *IEEE Journal of Quantum Electronics* , **QE-17**, 919 (1981).

4. D.S. Kliger, J.W. Lewis & C.E. Randall, *Polarized Light in Optics and Spectroscopy* , (Academic Press, Boston, 1990).

5. C. Salomon, D. Hills & J.L. Hall, *Journal of Optical Society of America B* , **5**, 1576-87 (1988).

6. A. Korpel, *Acousto-Optics* , (Marcel Dekker, New York, 1988).

7. N. Magdich & V.Y. Molchanov, *Acoustooptic Devices and Their Applications* , (Gordon and Breach, New York, 1989).

8. C.C. Barron, *et al.*, *IEEE Journal of Quantum Electronics* , **31**, 1484-93 (1995).

9. D.A.B. Miller, in *Trends in Optics 1995* , (Academic Press, 1995).

10. K. Kasahara, *Optical and Quantum Electronics* , **24**, 783-800 (1992).

11. W. Franz, *Z. Naturforsch* , **13a**, 484 (1958).

12. L.V. Keldysh, *Zh. Eksp. Teor. Fiz.* , **34**, 1138 (1958).

13. M.A. Herman & H. Sitter, *Molecular beam epitaxy : fundamentals and current status* , 1-453 (Springer, Berlin, 1996).

14. A.Y. Cho, *J. Crystal Growth* , **111**, 1-13 (1991).

15. D.A.B. Miller, *et al.*, *Applied Physics Letters* , **42**, 925 (1983).

16. D.A.B. Miller, *et al.*, *Physics Review B* , **32**, 1043-1060 (1985).

17. H.S. Hinton, *An introduction to photonic switching fabrics* , 1-525 (Plenum Press, New York, 1993).

18. B. Pezeshki, S.M. Lord, T. Boykin & J.S. Harris. Jr., *Applied Physics Letters* , **60**, 2779 (1992).

19. C. Cohen-Tannoudji, *Quantum Mechanics* , (Wiley, New York, 1977).

20. G.D. Boyd, L.M.F. Chirovsky, A.L. Lentine & G. Livescu, *Appl. Optics* , **34**, 323 (1995).

21. A.L. Lentine, *et al.*, *IEEE Journal of Quantum Electronics* , **25**, 1928-1936 (1989).

22. B. Pezeshki, D. Thomas & J.S. Harris, *Applied Physics Letters* , **57**, 1491 (1990).

23. B. Pezeshki, Ph.D. thesis, *Electrical Engineering,* (Stanford University, Stanford, 1991).

24. D.A.B. Miller, *et al.*, *IEEE Journal of Quantum Electronics* , **QE-21**, 1462 (1985).

25. G.D. Boyd, *et al.*, *Applied Physics Letters* , **50**, 1119 (1987).

26. M. Whitehead, A. Rivers, G. Parry, J.S. Roberts & C. Button, *Electronics Letters* , **25**, 984-985 (1989).

27. G. Hernandez, *Fabry-Perot interferometers* , (Cambridge University Press, Cambridge, 1986).

28. J.L. Jewell, J.P. Harbison, A. Schere, Y.H. Lee & L.T. Florez, *IEEE Journal of Quantum Electronics* , **27**, 1332 (1991).

29. C.J. Chang-Hasnain, in *Semiconductor Lasers: Past, Present, and Future* , (ed. Agrawal, G.P.) (AIP, 1995).

30. R.H. Yan, R.J. Simes & L.A. Coldren, *IEEE Journal of Quantum Electronics* , **25**, 2272 (1989).

31. R.H. Yan, R.J. Simes & L.A. Coldren, *IEEE Photonics Technology Letters* , **1**, 273-275 (1989).

32. K. Bacher, B. Pezeshki, S.M. Lord & J.S. Harris, *Applied Physics Letters* , **61**, 1387-9 (1992).

33. S.A. Chambers & K.P. Killeen, *Applied Physics Letters* , **62**, 1182-4 (1993).

34. H.A. Macleod, *Thin Film Optical Filters* , (Macmillan, New York, 1986).

35. S. Adachi, *Journal of Applied Physics* , **58**, R1 (1985).

36. J.D. Jackson, *Classical Electrodynamics* , (Wiley, New York, 1963).

37. G.D. Boyd & G. Livescu, *Optical and Quantum Electronics* , **24**, S147 (1992).

38. M.C. Larson, Ph.D. thesis, *Electrical Engineering,* (Stanford University, Stanford, 1996).

39. T. Li, *Optical Fiber Data Transmission,* (Academic Press, Boston, 1991).

40. W.B. Jones, *Introduction to optical fiber communication systems* , 1-347 (Holt, Rinehart & Winston, New York, 1987).

41. T.H. Wood, R.W. Tkach & A.R. Chraplyvy, *Applied Physics Letters* , **50**, 798 (1987).

42. C.H. Henry, *IEE Journal of Quantum Electronics* , **QE-19**, 228-31 (1982).

43. K. Koyama & K. Iga, *Electronics Letters* , **21**, 1065-6 (1985).

44. C. Harder, K. Vahala & A. Yariv, *Applied Physics Letters* , **42**, 328-30 (1983).

45. C.A. Green, N.K. Dutta & W. Watson, *Applied Physics Letters* , **50**, 1409-10 (1987).

46. F. Koyama & K. Iga, *Journal of Lightwave Technologies* , **6**, 87 (1988).

47. H. Soda, K. Sato, K. Nakai, H. Ishikawa & H. Imai, *Electronics Letters* , **24** (1988).

48. M.S. Whalen, *et al.*, *IEEE Photonics Technology Letters* , **3**, 451 (1991).

49. Y.H. Lee, *et al.*, *Applied Physics Letters* , **53**, 1684 (1988).

50. G. Livescu, G.D. Boyd, R.A. Morgan, L.M.F. Chirovsky & A.M. Fox, *Applied Physics Letters* , **60**, 1418 (1992).

51. D. Liu, B. Pezeshki, S.M. Lord & J.S. Harris, *Applied Physics Letters* , **62**, 2158 (1993).

52. B. Pezeshki, G.A. Williams & J.S. Harris. Jr., *Applied Physics Letters* , **60**, 1061 (1992).

53. J.A. Trezza, M.C. Larson & J.S. Harris, *Journal of Applied Physics* , **74**, 7061-6 (1993).

54. J.A. Trezza, B. Pezeshki, M.C. Larson, S.M. Lord & J.S. Harris, *Applied Physics Letters* , **63**, 452-4 (1993).

55. J.A. Trezza, J.S. Powell & J.S. Harris, *IEEE Photonics Technology Letters* , **9**, 330-2 (1997).

56. J.A. Trezza & J.S. Harris, in *Proceedings of 1994 Conference on Lasers and Electro-Optics and The International Electronics Conference CLEO/IQEC,* 376-7 (Anaheim, CA, USA, 1994).

57. J.A. Trezza & J.S. Harris, *Journal of Applied Physics* , **75**, 4878-84 (1994).

58. J.A. Trezza, in *Electrical Engineering,* (Stanford University, Stanford, 1995).

59. R.H. Yan, R.J. Simes & L.A. Coldren, *Applied Physics Letters* , **55**, 1946 (1989).

60. D. Liu, *Proceedings of 1994 CLEO/IQEC,* Vol. **8**, 171, (Anaheim, 1994).

61. A. Obeidat, J. Khurgin & S. Li, in *OSA Topical Meeting on Spatial Light Modulators,* (Palm Springs, 1993).

62. A. Obeidat, J. Khurgin & S. Li, *Optical and Quantum Electronics* , **25**, S917-S923 (1993).

63. B. Pezeshki, personal communication (1995).

64. I.J. Fritz, J.F. Klem & J.R. Wendt, *Applied Physics Letters* , **65**, 2093 (1991).

65. P. Zouganeli & G. Parry, *IEEE Journal of Quantum Electronics* , **31**, 1140-51 (1995).

66. R.P. Stanley, R. Houdre, U. Oesterle & M. Ilegems, *Applied Physics Letters* , **65**, 2093 (1994).

67. W.T. Tsang, in *Lightwave Communications Technology, Part B* , (ed. Tsang, W.T.), (Academic Press, Orlando, 1985).

68. G.P. Agrawal & N.K. Dutta, *Long Wavelength Semiconductor Lasers* , (Van Nostrand Reinhold, New York, 1986).

69. Z. Knittl, *Optics of Thin Films* , (John Wiley & Sons, London, 1976).

70. B.E. Saleh & M.C. Teich, *Fundamentals of Photonics* , (Wiley, New York, 1991).

71. E.F. Schubert, Y.-H. Wang, A.Y. Cho, L.-W. Tu & G.J. Zydzik, *Applied Physics Letters* , **60**, 921-3 (1992).

72. N.E.J. Hunt, *et al.*, *Applied Physics Letters* , **63**, 2600-2 (1993).

73. E.F. Schubert, N.E.J. Hunt, R.J. Malik, M. Micovic & D.L. Miller, *Journal of Lightwave Technology* , **14**, 1721-9 (1996).

74. B.A. Wilson, *IEEE Journal of Quantum Electronics* , **24**, 1763-77 (1988).

75. A.M. Fox, D.A.B. Miller, G. Livescu, J.E. Cunningham & W.Y. Jan, *IEEE Journal of Quantum Electronics* , **27**, 2281 (1991).

IMAGE EVALUATION TEST TARGET (QA-3)

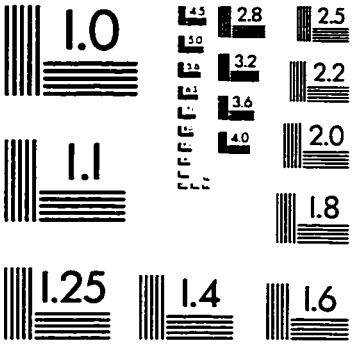

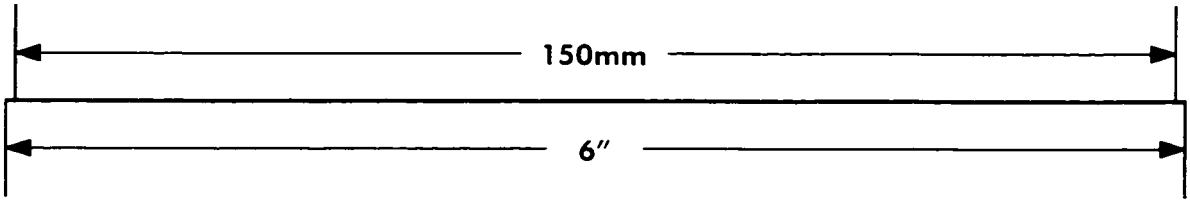

APPLIED IMAGE, Inc
1653 East Main Street
Rochester, NY 14609 USA
Phone: 716/482-0300
Fax: 716/288-5989